ACS Partner Journal
PRECISION CHEMISTRY
pubs.acs.org/PrecisionChem

Review

Growth of Noncentrosymmetric Two-Dimensional Single Crystals

Guoliang Cui,[#] Jiajie Qi,[#] Zhihua Liang,[#] Fankai Zeng,[#] Xiaowen Zhang, Xiaozhi Xu,[*] and Kaihui Liu[*]

Cite This: *Precis. Chem.* 2024, 2, 330−354

Read Online

ACCESS | Metrics & More | Article Recommendations

ABSTRACT: Among the various two-dimensional (2D) materials, more than 99% of them are noncentrosymmetric. However, since the commonly used substrates are generally centrosymmetric, antiparallel islands are usually inevitable in the growth of noncentrosymmetric 2D materials because of the energetic equivalency of these two kinds of antiparallel islands on centrosymmetric substrates. Therefore, achieving the growth of noncentrosymmetric 2D single crystals has long been a great challenge compared with the centrosymmetric ones like graphene. In this review, we presented the remarkable efforts and progress in the past decade, through precise chemical processes. We first discussed the great challenge and possible strategies in the growth of noncentrosymmetric 2D single crystals. Then, we focused on the advancements made in producing representative noncentrosymmetric 2D single crystals, including hexagonal boron nitride (hBN), transition metal dichalcogenides (TMDs), and other noncentrosymmetric 2D materials. At last, we summarized and looked forward to future research on the growth of layer-, stacking-, and twist-controlled noncentrosymmetric 2D single crystals and their heterostructures.

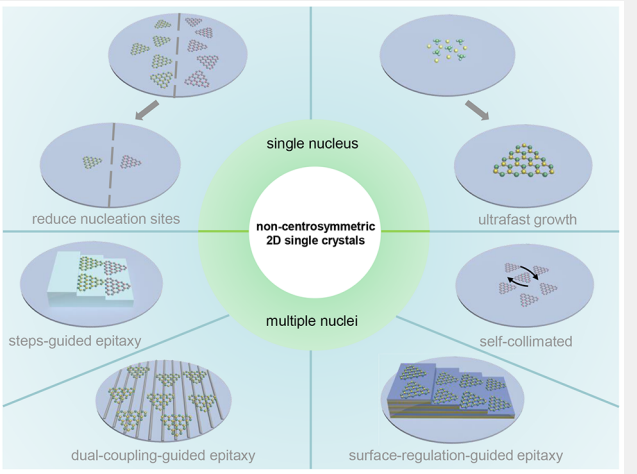

KEYWORDS: *noncentrosymmetric, two-dimensional materials, single crystals, hexagonal boron nitride, transition metal dichalcogenides*

1. INTRODUCTION

1.1. The Rise of Two-Dimensional (2D) Materials

2D materials are a class of materials that have a thickness of only a few atomic layers. In 2004, the first kind of 2D material, graphene, was mechanically exfoliated.[1] Since then, many different kinds of 2D materials have been discovered, including hexagonal boron nitride (hBN), transition metal dichalcogenides (TMDs, such as $MoSe_2$, MoS_2, $MoTe_2$, WSe_2, WS_2, ReS_2, and TaS_2), simple substances (such as phosphorene, silicene, and germanene), group III/V monochalcogenides (such as In_2Se_3, SnS, and GeSe), group III−IV binary compounds (such as GaN and GaAs), among others.

In contrast to the bulk materials, 2D materials confine electrons within a plane, leading to numerous distinctive properties and potential applications.[2] These materials provide excellent platforms for fundamental scientific exploration, enabling the uncovering of intriguing physical phenomena such as room temperature quantum Hall effect, Mott insulation state, anomalous superconductivity, and fractional quantum anomalous Hall effect.[3−6] Moreover, their high carrier mobility, adjustable bandgap, strong spin−valley coupling, robust light−matter interaction, large specific surface area, and short diffusion path make 2D materials highly promising candidates for next-generation electronics, optoelectronics, sensors, energy storage, catalysis, and biomedicine.[7−13]

1.2. Challenge in the Growth of Noncentrosymmetric 2D Single Crystals

For practical applications, achieving large 2D single crystals is a grail. The exceptional single crystallinity and absence of grain boundaries (GBs) in these crystals ensure their intrinsic physical and chemical properties, thereby guaranteeing ultimate performance and uniformity of devices. Numerous experimental studies and theoretical calculations have indicated that the presence of GBs in polycrystalline hBN and TMDs significantly restrict their electrical properties.[14−17] The defects and GBs serve as charge scattering sites and traps, hindering the advancement of high-performance electronics. Specifically, GBs in hBN are associated with conductive defects localized at the Cu and hBN grain boundaries. These defects can be

Special Issue: Precision Chemistry for Two-Dimensional Materials

Received: December 26, 2023
Revised: March 13, 2024
Accepted: March 18, 2024
Published: April 5, 2024

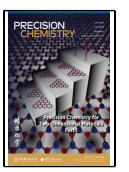

https://doi.org/10.1021/prechem.3c00122
Precis. Chem. 2024, 2, 330−354

visually observed through conductive atomic force microscopy (AFM) imaging, which reveals the distribution of conductive defects across hBN films (Figure 1a,b).[18] Such GBs in hBN are

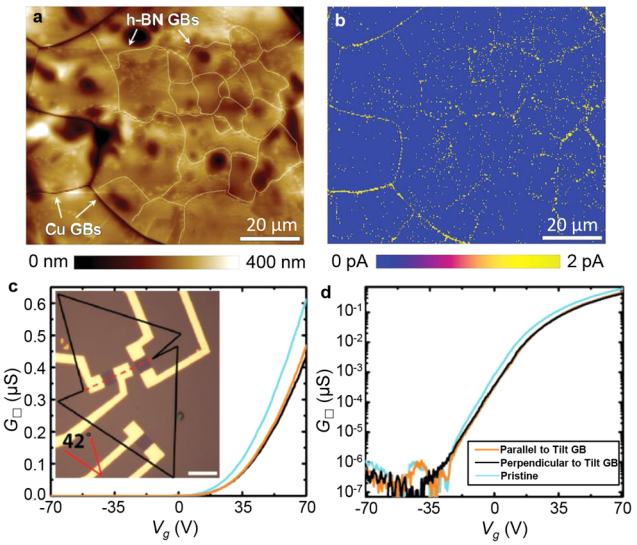

Figure 1. (a) Topographic and (b) current mapping of a polycrystalline hBN film (Reproduced from ref 18. Copyright 2021 Wiley). (c,d) Linear and logarithmic electrical transport transfer curves. (Reproduced from ref 20. Copyright 2013 Springer Nature).

inherently susceptible to electrical breakdown, chemical attack, or mechanical failure due to their atomic stitching structure. This renders monolayer hBN films ineffective for their intended applications as ultrathin dielectrics, barrier layers, or separation membranes. Additional evidence further demonstrates the detrimental effects caused by these GBs. Ly et al. measured the electrical transport of polycrystalline MoS_2 with a GB misorientation angle of 19°, the results reveal that the intradomain regions consistently exhibit higher μ_{FE} and reduced R_S compared to interdomain regions.[19] A similar trend is also observed in MoS_2 islands with tilted boundaries (Figure 1c). Both parallel and perpendicular devices experience a decrease of 30% in on-state boundary conductance when compared to pristine crystals (Figure 1d).[20] Furthermore, the susceptibility of grain boundaries to environmental degradation complicates their utilization in electronics. For instance, Wang et al. reported that GBs in $MoSe_2$ were etched under wet H_2O vapor exposure, highlighting their environmental instability.[21] These findings are crucial for applications requiring materials that are stable and reliable. Therefore, great efforts have been employed on the growth of 2D single crystals in the past decade.

Graphene is the first discovered 2D material, and the growth of single-crystal graphene with meter scale has been achieved now.[22−31] Highly aligned graphene islands can be obtained on Cu (111) due to the matched symmetry and small lattice mismatch.[32] In 2015, Nguyen et al. successfully synthesized a 6 × 3 cm^2 Cu (111) single crystal through repeated annealing and chemical mechanical polishing, enabling the growth of aligned graphene islands (Figure 2a,b).[33] Furthermore, in 2017, Xu et al. developed a temperature-gradient-driving annealing method to produce meter-scale Cu (111) foils (Figure 2c) and achieved the largest single-crystal graphene within just 20 min using an ultrafast epitaxial growth technique (Figure 2d).[22] Monolayer graphene single crystals have also been successfully grown on high-index Cu surfaces, including Cu (112), Cu (113), Cu (133), Cu (311), and Cu (436).[34−36] Additionally, substrates like Ge (110), Ge (001), Pt (111), and CuNi (111) can also be utilized.[37−40] For instance, Lee et al. and Li et al. synthesized wafer-scale single-crystal graphene on Ge (110) and 15° miscut Ge (001) substrates by precisely arranging all graphene islands, respectively (Figure 2e−h).[37,38] Kang et al. reported the production of 6-in. single-crystal graphene on Pt (111) substrates through ambient-pressure chemical vapor deposition (CVD), as shown in Figure 2i−k.[39] Deng et al., on the other hand, enhanced the catalytic activity of Cu by introducing a small amount of Ni and successfully prepared a 4-in. monolayer single-crystal graphene wafer on $Cu_{90}Ni_{10}$ (111) substrates in just 10 min (Figure 2l−n).[40] Overall, significant advancements have been made in the production of large graphene single crystals.

Unlike the growth of graphene, synthesizing single-crystal noncentrosymmetric 2D materials like hBN and TMDs is very challenging. In general, the commonly used substrates are centrosymmetric, resulting in only one orientation for centrosymmetric 2D materials (Figure 3a). When these islands merge together, they will be seamlessly stitched into single-crystal films. In contrast, the noncentrosymmetric 2D materials possess two energetically favorable antiparallel orientations. When these islands merge, grain boundaries will be formed (Figure 3b). For this reason, all of the earlier works could only produce antiparallel islands (Figure 3c−g).[41−44]

This review offers a comprehensive overview of the production of noncentrosymmetric 2D single crystals. First, we discussed the growth strategy of noncentrosymmetric 2D single crystals. Subsequently, our focus shifts toward the controlled growth methodologies applied to hBN, TMDs, and other representative noncentrosymmetric 2D materials. Lastly, we provide a concise summary of the challenges faced in this field and highlight intriguing avenues for future exploration.

2. GROWTH STRATEGY OF NONCENTROSYMMETRIC 2D SINGLE CRYSTALS

Under natural circumstances, 2D materials tend toward multinucleus growth with random orientations, resulting in the formation of polycrystalline films. This growth behavior is independent of the substrate materials. To obtain large 2D single crystals, stringent control is necessary. Generally, there are two strategies to produce single-crystal 2D materials: single-nucleus growth and multinuclei growth. For the growth from a single nucleus, the key is to reduce the nucleation density, allowing the growth of 2D materials from a single nucleus to a large-sized single crystal. For the growth from multiple nuclei, strict control of the nucleation density is not necessary, the key here is to accurately control the lattice orientations of the islands grown from different nuclei. If all islands possess identical lattice orientations, then these islands can be seamlessly stitched into large single-crystal films.

2.1. Growth from a Single Nucleus

Effective control of nucleation during the initial growth stage is very important in determining the size and quality of single-crystal 2D materials. During the growth process, precursors tend to adsorb on defects, boundaries, particles, and other high-energy regions of the substrate, leading to nuclei formation with varying orientations.[45−48] To reduce the nucleation density, one way is to resolidify the metal substrate.[49,50] This melting process eliminates high-energy sites on the surface, resulting in an atomic flat surface and low nucleation density (Figure 4a).

https://doi.org/10.1021/prechem.3c00122
Precis. Chem. 2024, 2, 330−354

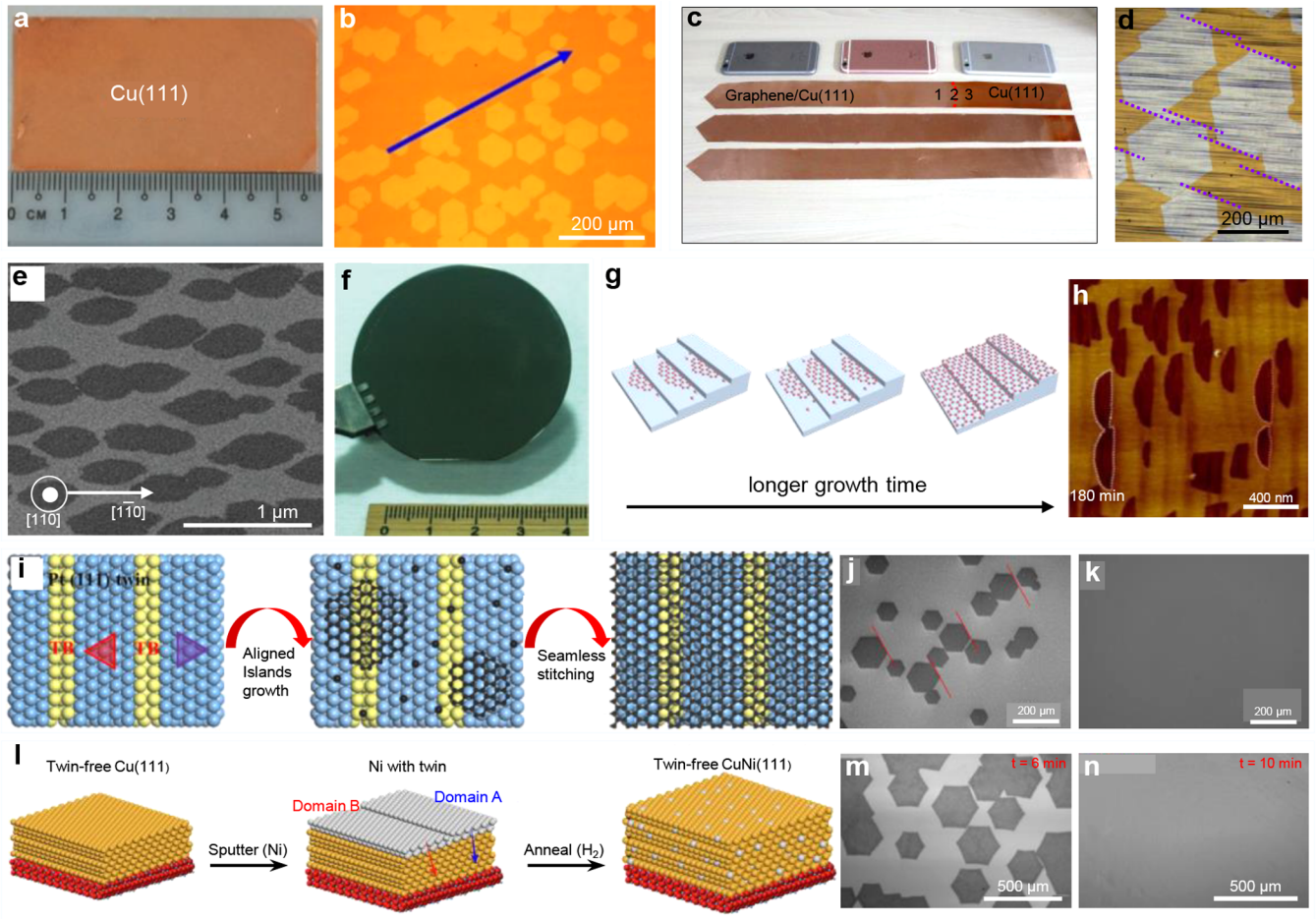

Figure 2. (a) Photograph of monocrystalline Cu (111). (b) Aligned graphene islands on Cu (111). (Reproduced from ref 33. Copyright 2015 Wiley). (c) Cu (111) foils covered with graphene. (d) Optical image of aligned graphene islands on Cu (111). (Reproduced from ref 22. Copyright 2017 Elsevier). (e) SEM image of graphene islands on Ge (110). (f) A photograph of the graphene wafer. (Reproduced from ref 37. Copyright 2014 American Association for the Advancement of Science). (g) Schematic diagrams of the growth process of single-crystal monolayer graphene. (h) AFM images of graphene islands on Ge (001). (Reproduced from ref 38. Copyright 2020 Elsevier). (i) Schematic of the growth of single-crystal graphene. (j,k) SEM images of graphene grown on Pt (111). (Reproduced from ref 39. Copyright 2021 Elsevier). (l) Schematic diagrams for the growth of single-crystal $Cu_{90}Ni_{10}$ (111). (m,n) SEM images of graphene with different coverage. (Reproduced from ref 40. Copyright 2019 Elsevier).

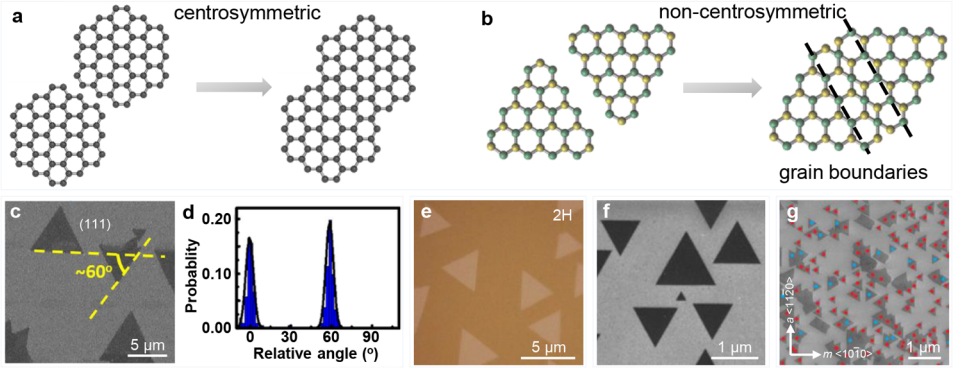

Figure 3. (a,b) Schematic diagrams of centrosymmetric (a) and noncentrosymmetric (b) 2D materials when rotating for 180°. Grain boundaries will be formed for noncentrosymmetric 2D materials. (c) SEM images of hBN islands on Cu (111). (d) Statistical distributions of the edge angles of hBN islands. (Reproduced from ref 41. Copyright 2015 Springer Nature). (e) Optical image of 2H MoS_2 monolayer flakes grown on mica. (Reproduced from ref 42. Copyright 2018 Springer Nature). (f) SEM images of MoS_2 islands on GaN. (Reproduced from ref 43. Copyright 2016 American Chemical Society). (g) SEM images of WSe_2 islands with antiparallel orientations. (Reproduced from ref 44. Copyright 2023 Springer Nature).

Another effective method is minimizing the amount of source as it makes nucleation more challenging and can effectively reduce the nucleation density. In addition to these methods, introducing additional elements such as oxygen has been found to significantly inhibit nucleation and facilitate large-sized single crystals.

Increasing the growth rate is another effective aspect of single-nucleus growth. Since the nucleation is a random event, the

https://doi.org/10.1021/prechem.3c00122
Precis. Chem. 2024, 2, 330−354

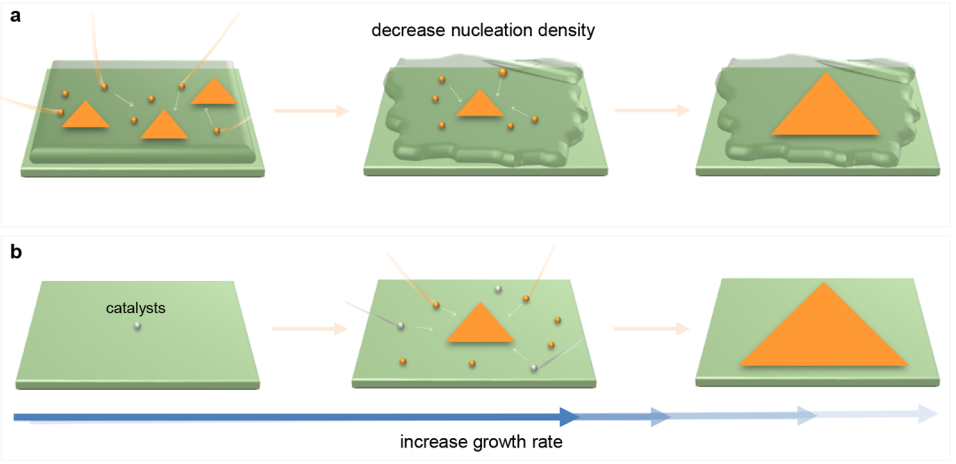

Figure 4. Schematic diagrams of single-crystal growth from a single nucleus by decreasing the nucleation density (a) and increasing the growth rate (b).

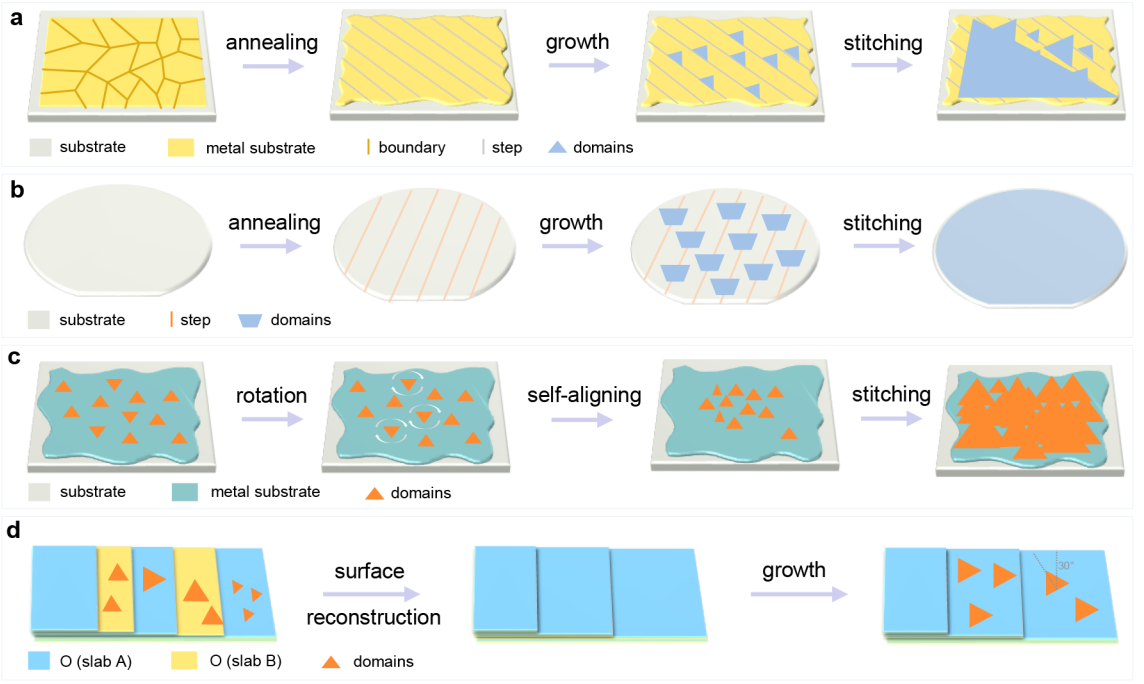

Figure 5. Schematic diagrams of single-crystal growth from multiple nuclei. (a) Steps-guided epitaxy on metal substrates. (b) Dual-coupling-guided epitaxy on insulating substrate. (c) Self-collimation growth on molten substrates. (d) Surface reconstruction to guarantee single-crystal epitaxy.

shorter the growth time, the less additional random nucleation will occur. So, one can obtain large-sized single crystals in a very short time (Figure 4b).[51]

2.2. Growth from Multiple Nuclei

A promising strategy for achieving the growth of wafer-scale noncentrosymmetric 2D single crystals is seamlessly stitching together 2D islands with identical orientation. However, when noncentrosymmetric materials grow on high-symmetric surfaces, the emergence of antiparallel islands is inevitable.[52−55] After a large number of attempts, there are currently four representative methods to achieve the orientation control of noncentrosymmetric 2D materials.[53−61]

The first mechanism is the step-guided epitaxy. Extensive studies indicate that the steps on substrate are critical for adjusting orientations of as-grown islands. Parallel and flat atomic steps can be produced on the surface of single-crystal metal substrates after high-temperature annealing. These parallel steps have a significant impact on reducing the nucleation barriers and inhibiting upper step growth. These two aspects guarantee only one edge of the 2D materials aligned with the step edges, ensuring the single-crystal direction (Figure 5a).[62,63]

The second mechanism is known as dual-coupling-guided epitaxy. Because the interaction between insulating substrates and 2D materials is much smaller than that between the metal substrate and the 2D materials. The presence of the steps cannot completely dominate the growth behaviors of these materials. In this case, a combination of van der Waals (vdW) interaction and steps interaction governs the growth mechanism, where the vdW interaction leads to two favored antiparallel orientations, while the steps interaction limits them to only one orientation. Consequently, these two interactions lead to the unidirectional alignment of the noncentrosymmetric 2D materials (Figure 5b).

https://doi.org/10.1021/prechem.3c00122
Precis. Chem. 2024, 2, 330−354

Growth on the surface of molten metal is another technique for preparing single crystals. This method utilizes a synergistic self-collimation mechanism, which combines CVD growth kinetics with the rheological kinetics on the molten metal surface. As a result, triangular crystal islands floating on the surface can be rotated toward the same orientation. These islands then align themselves spontaneously due to mutual atomic attraction, leading to an aligned orientation and seamless stitching over a large area (Figure 5c).[58]

The final approach to tune the orientations of the noncentrosymmetric 2D materials is to reconstruct the surface of the substrates and this method does not need the existence of the steps. For instance, when 2D grains interact with the exposed oxygen−aluminum atomic surface, they can form an energy-optimized configuration known as a 2D grain-sapphire structure. By reconstructing sapphire substrates to consist solely of a single type of atomic plane, it is also possible to ensure single-crystal epitaxy of monolayer noncentrosymmetric 2D materials (Figure 5d).[55]

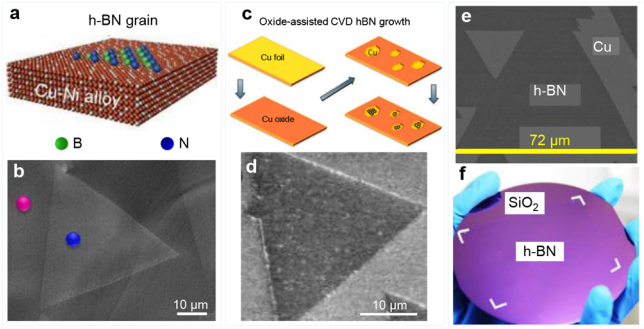

Figure 6. (a) Schematic diagram of hBN growth on Cu−Ni alloy. (b) SEM image of an hBN island. (Reproduced from ref 78. Copyright 2015 Springer Nature). (c) Schematic illustrations of the mechanism of hBN growth on preoxidized Cu. (d) SEM image of an hBN island. (Reproduced from ref 81. Copyright 2017 American Chemical Society). (e) SEM image of a large-domain hBN triangle. (f) Wafer-scale monolayer hBN film. (Reproduced from ref 41. Copyright 2015 Springer Nature).

3. GROWTH OF SINGLE-CRYSTAL HBN

hBN is a well-established noncentrosymmetric 2D materials, characterized by an alternating arrangement of boron and nitrogen atoms in its lattice. Its exceptional properties, including strong insulation, large nonlinear susceptibility, excellent chemical inertness, high thermal conductivity, and atomic flatness without dangling bonds make it highly suitable for potential applications in nanoelectronics, integrated photonics, quantum optics, and metal-corrosion protection.[64−72] To realize such applications of hBN from lab to industry, the production of large-sized single-crystal hBN films is a prerequisite. Since the hBN films were synthesized through the CVD method on the nickel foils, significant efforts have been dedicated to produce hBN single crystals in the past decades.[73−75]

3.1. Growth of Single-Crystal hBN from a Single Nucleus

When hBN islands originating from different nuclei with random lattice orientations merge together, grain boundaries would be inevitably formed. Therefore, one straightforward approach to achieve hBN single crystals is to decrease the nucleation density and make the single nucleus grow up.

One widely employed approach is to pretreat the epitaxy substrate surface to suppress or passivate the nucleation sites, such as the steps and grain boundaries. Thus, utilizing electrochemically polished or secondary recrystallized metal substrates with smoother surfaces can effectively enhance the size of hBN islands.[76,77] Additionally, doping other elements into the substrates has been proven to be an effective method. In 2015, Lu et al. introduced some Ni into Cu foils, resulting in a significant suppression of nucleation at both initial and subsequent growth stages (Figure 6a).[78] As a result, the nucleation density was decreased to 60 mm^{-2}, leading to an increase in the hBN island size to 7500 μm^2 (Figure 6b). This alloying strategy also yielded favorable results on Si-doped Fe and Cu−Si substrates.[79,80] Another effective approach for surface treatment is to preoxidize the epitaxy substrate before hBN growth. Taking Cu as an example, Chang et al. increased the binding energy of boron- and nitrogen-containing species by constructing a thin oxide layer on the Cu surface (Figure 6c).[81] This resulted in a reduction of nucleation density from 10^6 to 10^3 mm^{-2}, while improving the size of hBN islands to ∼20 μm (Figure 6d). Besides the formation of oxide layers, mild oxidation of the Cu foil can be achieved by introducing the trace O_2 in Ar gas during the heating step. For example, Li et al. introduced copper oxide nanoparticles onto the surface.[82] Typically, the nucleation density of hBN was highly limited down to 10^3 mm^{-2} by the number of nanoparticles, and the largest island size was observed to be more than 200 μm.

Another approach to decrease the nucleation density is to limit the supply of boron- and nitrogen-containing precursors, typically achieved by folding the metal foil to create an enclosure and utilizing its inner surface as the growth substrate. In 2015, Song et al. reported their synthesis of a wafer-scale hBN monolayer, where a single island size is about ∼72 μm (Figure 6e).[41] Moreover, they successfully transferred the monolayer film onto a target substrate like SiO_2/Si wafer by the PMMA-assistant technique (Figure 6f). Furthermore, a larger hBN island with an edge length of ∼300 μm has been obtained by selecting an appropriate thickness of Cu foil.[83] The utilization of the Cu enclosure could effectively reduce the nucleation density, while it would naturally decrease the precursor feeding rate, leading to a relatively lower production efficiency. To balance the growth rate and lateral size, Zhu et al. used a Cu−Ni gradient alloy enclosure to suppress the diffusion and enhance the decomposition to facilitate the growth of hBN and realized the lateral size of ∼60 μm.[84] Furthermore, the effective modulation of nucleation density and growth kinetics can also be realized by introducing a suitable atmosphere such as hydrogen,[85] ammonia,[86] and water,[87] or active species like fluorine.[88]

3.2. Growth of Single-Crystal hBN from Multiple Nuclei

Despite extensive exploration of nucleation control, the largest island size of single-crystal hBN remains limited to the submillimeter scale. As a result, while the grain boundaries can be dramatically reduced but inevitably exist when these islands coalesce within a wafer range. In order to achieve unidirectionally aligned growth of hBN islands, it is essential to tune the symmetry of the substrate.[52] Wang et al. have predicted that tilting the Cu (101) facet along specific in-plane axes to form inclined surfaces can effectively tune the lattice symmetry and realize the single favored hBN orientation.[89] This is consistent with the experimental result of aligned hBN islands grown on the Cu (102) and (103) surfaces.[90] This approach is anticipated to be further developed with the availability of various high-index Cu foils.[34]

https://doi.org/10.1021/prechem.3c00122
Precis. Chem. 2024, 2, 330−354

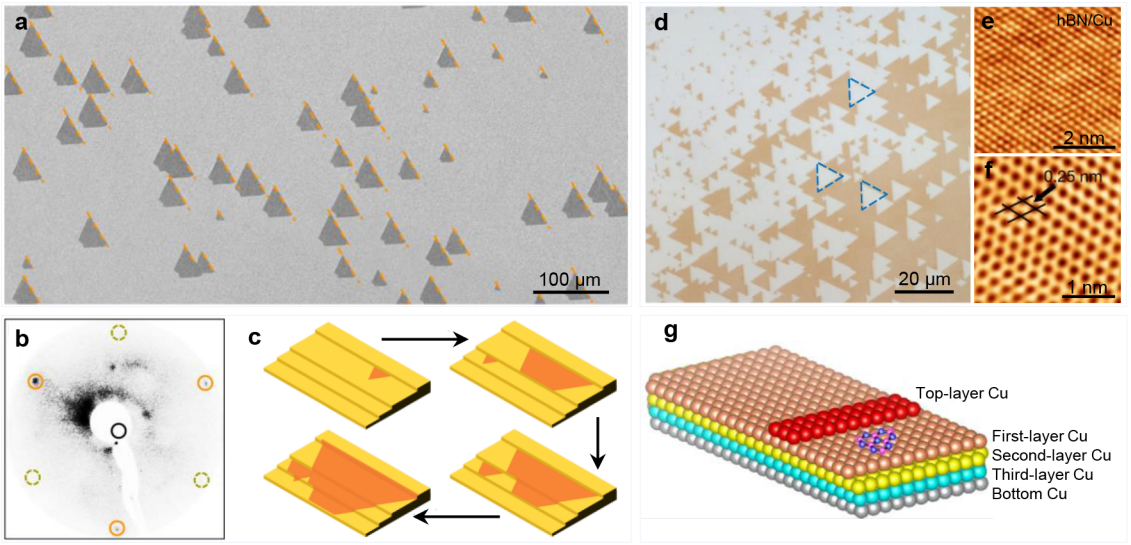

Figure 7. (a) SEM image of aligned hBN islands on Cu (110). (b) LEED pattern of hBN. (c) Schematic diagram of the growth process. (Reproduced from ref 56. Copyright 2019 Springer Nature). (d) Optical image of aligned hBN islands on Cu (111). (e,f) Atomic-scale STM images of hBN/Cu (111). (g) Theoretically calculated configurations. (Reproduced from ref 57. Copyright 2020 Springer Nature).

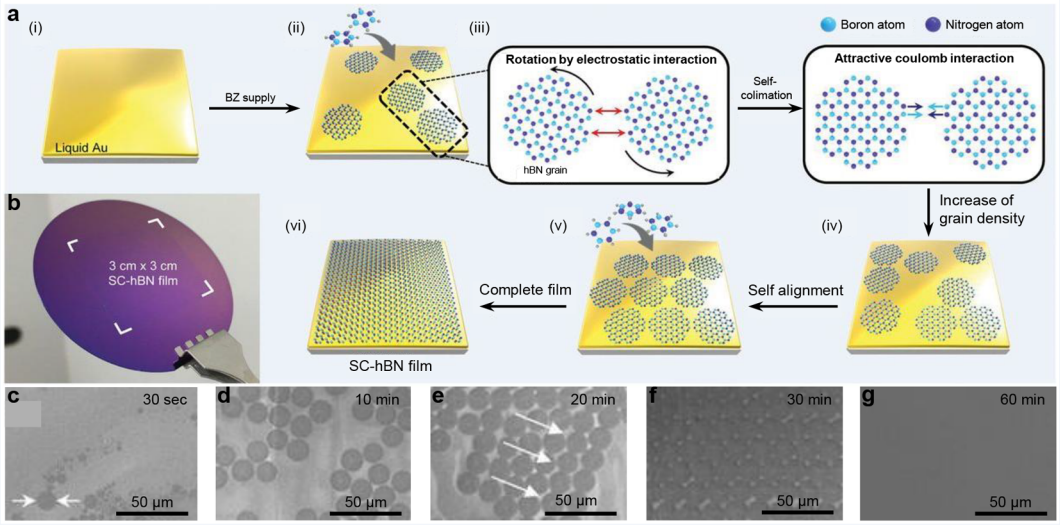

Figure 8. (a) Schematic diagrams of the growth process of single-crystal hBN. (b) A photograph of a single-crystal hBN film. (c–g) SEM images of hBN at different growth time. (Reproduced from ref 58. Copyright 2018 American Association for the Advancement of Science).

3.2.1. Step-Guided Epitaxy on Single-Crystal Substrates. The modulation of the hBN orientation is highly dependent on the strength of the vdW interaction between hBN and substrates, which might be relatively more susceptible to interference from external conditions. Single-crystal substrates with low-index surfaces, including (100), (110), and (111), are generally easier to obtain. Therefore, it is crucial to explore feasible methods for breaking the high lattice symmetry of these substrates and reliably locking the hBN orientation. Among these methods, constructing the atomic metal steps is a good choice.

In 2019, Wang et al. achieved the successful alignment of hBN islands and subsequently achieved the growth of single-crystal films.[56] Through the well-designed annealing process, they were able to obtain a 100 cm^2 single-crystal Cu foil with vicinal (110) surface and atomic steps along ⟨211⟩ direction. Then unidirectional hBN islands with truncated triangle shapes were grown within the entire area (Figure 7a), with an alignment exceeding 99%. The same crystalline orientation was further confirmed by the low-energy electron diffraction (LEED) patterns collected at the multiple positions (Figure 7b). *In situ* SEM was used to monitor the growth behavior of single-crystal hBN, including the unidirectionally aligned nucleation alone the parallel steps, the anisotropic growth on the Cu surface, and seamless stitching into a large-sized single crystal (Figure 7c). This work demonstrated that the artificially constructed steps could effectively reduce the lattice symmetry of Cu (110) surface to C_1, and the strong steps coupling between Cu and hBN enables the breaking of the energetic degeneracy of antiparallel hBN islands to finally achieve the production of single-crystal hBN monolayers.

Moreover, the step-modulation method can also be employed to hBN grown on Cu (111). Chen et al. reported the successful preparation of single-crystal hBN monolayers on Cu (111)

https://doi.org/10.1021/prechem.3c00122
Precis. Chem. 2024, 2, 330−354

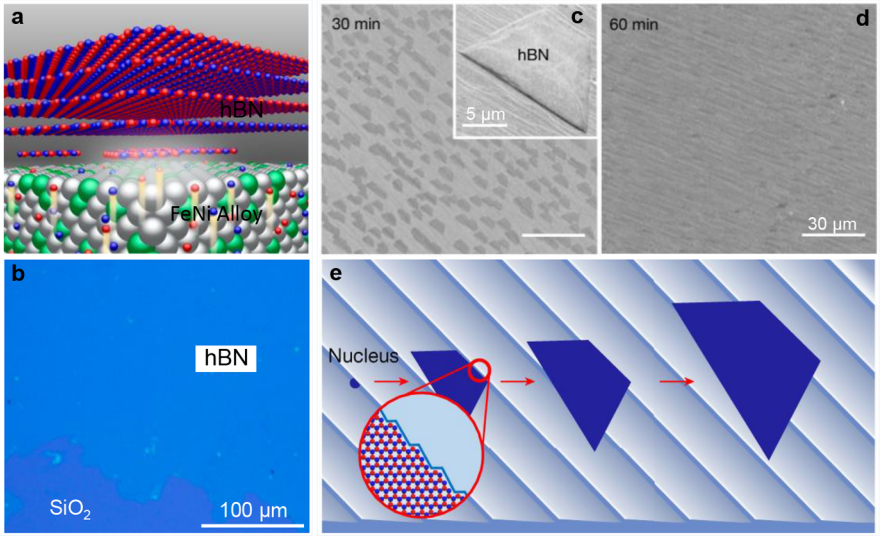

Figure 9. (a) Schematic of the growth process. (b) Optical image of hBN grown on Ni−Fe film. (Reproduced from ref 111. Copyright 2018 American Chemical Society). (c,d) SEM images of trilayer hBN islands at different growth time. (e) Illustration of hBN complementarity nucleation and growth process. (Reproduced from ref 62. Copyright 2022 Springer Nature).

(Figure 7d).[57] The atomic-resolution scanning tunneling microscopy (STM) characterizations show that the as-grown hBN on Cu (111) possessed the perfect crystal lattice (Figure 7e,f), exhibiting consistent lattice orientation over a wide range. Density functional theory (DFT) calculations were performed to reveal that this unidirectionally epitaxy was ensured by the lateral docking of hBN islands to the Cu (111) step edges (Figure 7g).

3.2.2. Self-Collimated Growth on Liquid Substrates. In addition to the introduction of metal steps, the symmetry of the substrate can also be broken on noncrystalline liquid metals. In 2015, Tan et al. successfully synthesized the self-aligned hBN arrays on a liquid Cu surface with uniform island sizes and consistent spatial orientations.[91] Furthermore, Lee et al. proposed a self-collimation mechanism for growing wafer-scale monolayer hBN single crystals through the seamless stitching of hBN islands on a liquid Au surface (Figure 8a).[58] The substrate was liquefied at an elevated temperature above the melting point of Au. The low solubility of B and N in Au ensured the high diffusion on such a flat surface to form isotropic circular hBN islands with a regular size of ∼14.5 μm. Afterward, the attractive Coulomb interaction between B and N atoms at the edge of different islands induced their rotation into a same orientation, and eventually stitched into single-crystal film (Figure 8b). The time-evolution SEM images captured at different growth stages comprehensively demonstrated the process of nucleation, lateral growth, coalescence, and full coverage (Figure 8c−g). The self-collimated synthesis technique was further developed by using a flowing liquid Cu surface.[59] By synergistically controlling CVD growth kinetics and liquid Cu rheological kinetics, floating triangular hBN islands could efficiently self-align by rotation, and a centimeter-scale uniform quasi-single-crystal hBN film was finally obtained.

3.3. Growth of Multilayer hBN

Multilayer hBN not only integrates the exceptional properties of its monolayer counterpart but also exhibits additional unique ones beyond monolayers, including stacking-dependent optical nonlinearity and interfacial ferroelectricity,[92−96] the ability to prevent leakage and breakdown,[97,98] as well as the infrared hyperbolic phonon polariton.[99,100] In the past years, many kinds of attempts have been tried to synthesize the homogeneous large-scale hBN multilayers, including ion beam sputtering deposition (IBSD),[101] molecular beam epitaxy (MBE),[102−105] and metal−organic chemical vapor deposition (MOCVD),[106] among which CVD is the most commonly used approach. However, a major challenge arises from the low solubility of B or/and N in epitaxial substrates, which dominates the self-limited growth mechanism of BN and hinders adlayer formation. To overcome this limitation, substrates with high solubility of B and N as well as long-range catalytic ability are extensively employed, leading to the development of various growth modes as discussed below.

Highly catalytic active Pt was used to grow hBN multilayers, but its high cost hindered its further development.[107] Polycrystalline Ni with the relatively high solubility of B atoms was first chosen as the substrate and realized the growth of multilayer hBN films with the thickness ranging from ∼5−50 nm.[73] Further investigations revealed a linear dependence between the average thickness of hBN films and growth time, allowing for tunability from a few to several hundred layers.[74] Besides Ni, Fe is another suitable substrate due to its high N solubility (∼8.0 atom % at 1000 °C) and its ability to readily react with B atoms, which can be dissolved into the Fe through a reaction-diffusion mechanism.[108,109] Kim et al. synthesized the 3 × 3 cm^2 multilayer hBN films with thickness up to 15 nm on Fe.[110] The growth was mainly governed by the segregation of B and N atoms from iron bulk, rather than the surface-mediated Frank−van der Merwe model since the thickness and grain size were strongly dependent on the cooling rate. However, achieving a smooth surface for single crystal Fe poses a significant challenge due to its phase transition from a body-centered cubic (bcc) to face-centered cubic (fcc) structure at ∼912 °C. This naturally leads to the nonuniform precipitation and growth of hBN on the substrate. In 2018, Uchida et al. introduced the Ni atoms into Fe substrates to stabilize the fcc structure and adjust the solubility of B and N atoms, to finally realize the homogeneous segregation of hBN multilayers (Figure 9a,b).[111] Fukamachi et al. successfully obtained a centimeter-scale multilayer hBN film with an average thickness

https://doi.org/10.1021/prechem.3c00122
Precis. Chem. 2024, 2, 330−354

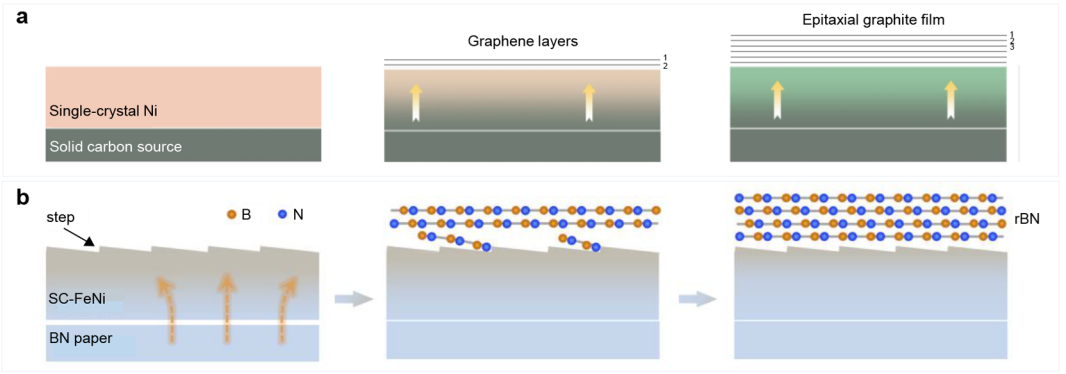

Figure 10. (a) Schematic diagrams for the continuous epitaxial growth of graphite. (Reproduced from ref 117. Copyright 2022 Springer Nature). (b) Schematic diagrams for the continuous epitaxial growth of rBN. (Reproduced from ref 118. Copyright 2023 Wiley).

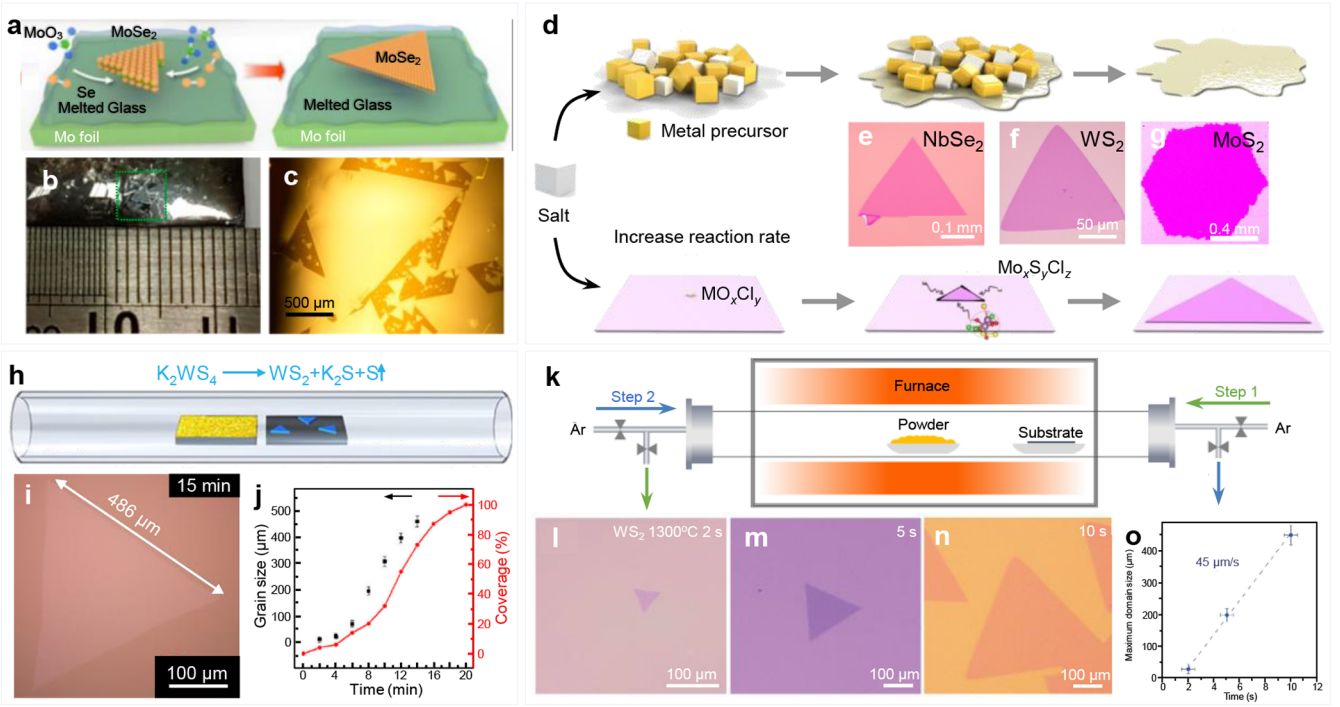

Figure 11. (a) Schematic diagrams for the production of $MoSe_2$ monolayers. (b,c) Photograph and optical image of $MoSe_2$ islands. (Reproduced from ref 50. Copyright 2017 American Chemical Society). (d) Schematics of the reactions. (e–g) Optical images of different TMDs monolayers. (Reproduced from ref 125. Copyright 2018 Springer Nature). (h) Schematic diagram for the set up. (i) Optical image of a WS_2 island. (j) The evolution of domain size and coverage of the WS_2 with growth time. (Reproduced from ref 126. Copyright 2020 Springer Nature). (k) Schematic illustration of a modified CVD system with reverse flow. (l–n) Optical images of WS_2 synthesized at different times. (o) The maximum island size of WS_2 as a function of growth time. (Reproduced from ref 132. Copyright 2020 Oxford University Press).

of ~6 nm and a low surface roughness of 0.19 nm by optimizing the growth parameters.[112] In fact, during the epitaxial growth of single-crystal 2D materials, the orientation of the 2D lattice is closely associated with lattice matching and substrate surface steps, while the catalytic activity of the substrate primarily influences growth rate and nucleation through precursor decomposition and dissolution.[113−116] It can be inferred that catalytic features of substrates play a secondary role in determining both the structure of the two-dimensional lattice and subsequent grain boundary formation. Therefore, all aforementioned hBN films are nonuniform and polycrystalline with massive grain boundaries, which hinder their high-end and industrial-level applications. Recently, Ma et al. realized the epitaxy of a 2 × 5 cm^2 multilayer hBN single crystal with precisely controlled thickness on a stepped Ni (111) substrate.[62] As shown in Figure 9c, the trilayer hBN nuclei were unidirectionally arranged on the Ni surface, and then synchronically grew up and seamlessly merged into a uniform single crystal (Figure 9d). Detailed AFM characterization and DFT calculation showed that the nucleation was guided by the Ni steps (Figure 9e).

The production of thick hBN is also required in many scenarios. The solid substrates with a well-defined lattice structure may be a possible way. In 2022, Zhang. et al. reported the continuous epitaxial growth of centimeter-size single-crystal graphite films with thickness up to 100,000 layers on single-crystal Ni (520) foils by the isothermal dissolution−diffusion−precipitation (IDDP) process of carbon atoms (Figure 10a).[117]

https://doi.org/10.1021/prechem.3c00122
Precis. Chem. 2024, 2, 330−354

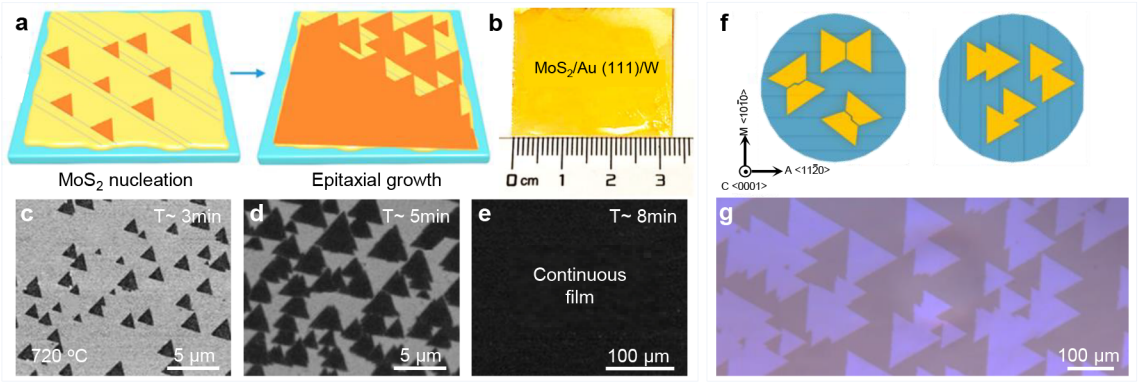

Figure 12. (a) Schematic diagrams for the growth of single-crystal MoS_2 on Au (111). (b) A photograph of the MoS_2/Au (111). (c–e) SEM images of aligned MoS_2 islands with different growth time. (Reproduced from ref 60. Copyright 2020 American Chemical Society). (f) Schematic diagrams of MoS_2 islands on C/M and C/A sapphire (0001). (g) Optical image of MoS_2 islands. (Reproduced from ref 54. Copyright 2021 Springer Nature).

Subsequently, this groundbreaking study was followed by the synthesis of uniform rhombohedral boron nitride (rBN) crystalline film using the same IDDP mechanism.[118] To achieve this, single-crystal FeNi alloys which were chosen as the epitaxial substrate due to the high solubility of both boron and nitrogen. At the elevated temperature, the B and N atoms would continuously dissolve into the bottom surface of the FeNi alloy, diffuse through the whole metal, and finally precipitate on the top surface to layer-by-layer form the BN multilayers with the thickness up to 1 μm (Figure 10b).

4. GROWTH OF SINGLE-CRYSTAL TMDS

2D TMDs have attracted great research interest due to the potential applications in the fields of electronics, optoelectronics, electrocatalysis, etc.[119−121] To meet the requirements of high-end applications, it is necessary to prepare high-quality single-crystal TMDs with low-density defects.

4.1. Growth of Single-Crystal TMDs from a Single Nucleus

Currently, available TMDs usually exhibit uncontrolled layer number, small single-crystal size, and low growth rate.[122] Achieving the growth of large monolayer TMDs single crystals is a fundamental challenge. It requires maximizing lateral growth rates while reducing the density as much as possible and has inspired considerable efforts.

As commonly accepted, the nucleation tends to occur preferentially at the impurities and defects on the solid substrate. To promote the growth of large single crystals, complex procedures or surface treatments are necessary to inhibit the nucleation.[48] In 2017, Chen et al. demonstrated the successful growth of millimeter-sized monolayer $MoSe_2$ on molten glass using an ambient pressure CVD system (Figure 11a).[50] The melting and subsequent regeneration of the glass result in a smooth surface. This "liquid-state" glass has an isotropic surface that significantly reduces the defects and enables low-density nucleation for large island growth. $MoSe_2$ islands with large size (~2.5 mm) and high carrier mobility (~95 $cm^2 V^{-1}·s^{-1}$) at room temperature can be synthesized quickly (Figure 11b,c). Additionally, it demonstrates the universality of this approach by successfully synthesizing millimeter-sized monolayer MoS_2 as well.

In addition, the production of many TMDs is challenging due to high melting points of the metal oxide precursors. To address this issue, molten salt-assisted methods have emerged to promote the growth of monolayer MoS_2, WS_2, and WSe_2.[123,124] In 2018, Zhou et al. reported the universality of molten salt-assisted CVD (Figure 11d) for synthesizing various TMDs.[125] They successfully synthesized 47 compounds, including 32 binary compounds, 13 alloys, and two heterostructural compounds (Figure 11e–g). The presence of salt enables reactions with specific metal oxides to form metal chloride oxides that evaporate at lower temperatures, thus promoting the growth of 2D TMDs. During the growth process, a stable nucleus is formed through coarsening, and then adsorbed atoms and clusters of chalcogenide elements and metals attach to the edges of the growing 2D monolayer, exhibiting rapid growth.

Choosing a different type of precursor may offer a more direct and convenient route. Zhou et al. developed a controlled method for monolayer WS_2 growth by CVD using K_2WS_4 as the precursor (Figure 11h).[126] Unlike the use of WO_x (x denotes the number of atoms) and S as precursors, this approach solely involves the thermal decomposition reaction of K_2WS_4, thereby enhancing the controllability of WS_2 growth. The simple chemistry employed by this method improves controllability and allows for rapid growth rates of about 30 μm/min. This enables the growth of monolayer WS_2 flakes up to ~500 μm with low defect density, which exhibit superior electrical properties compared to the single crystals grown by prior methods (Figure 11i,j).

In the CVD process, reducing nucleation density is typically achieved by minimizing the feeding rate to minimize the probability of nucleation probability.[127] But this significantly reduces the lateral growth rate (usually ~1 μm/s or less).[128] The growth of large monolayers often needs a long growth time, sometimes spanning hours or even longer to achieve millimeter-scale monolayers.[129] Producing large single crystals with high growth rates is a key challenge in 2D crystal growth.[130,131] In 2020, Zhang et al. used a counter-current reactor to achieve well-controlled nucleation and growth at high temperatures, thereby achieving ultrafast growth of large monolayer TMD single crystals (Figure 11k).[132] Specifically, a reverse airflow is used during increasing the temperature to prevent accidental nucleation. This method effectively prevents nucleation and growth before the optimal growth temperature is reached. This, in turn, guarantees a plentiful supply of gas-phase reactants and adequate surface mobility, facilitating the fast growth. It is possible to obtain a maximum lateral growth rate of 45 μm/s (Figure 11i–o).

https://doi.org/10.1021/prechem.3c00122
Precis. Chem. 2024, 2, 330−354

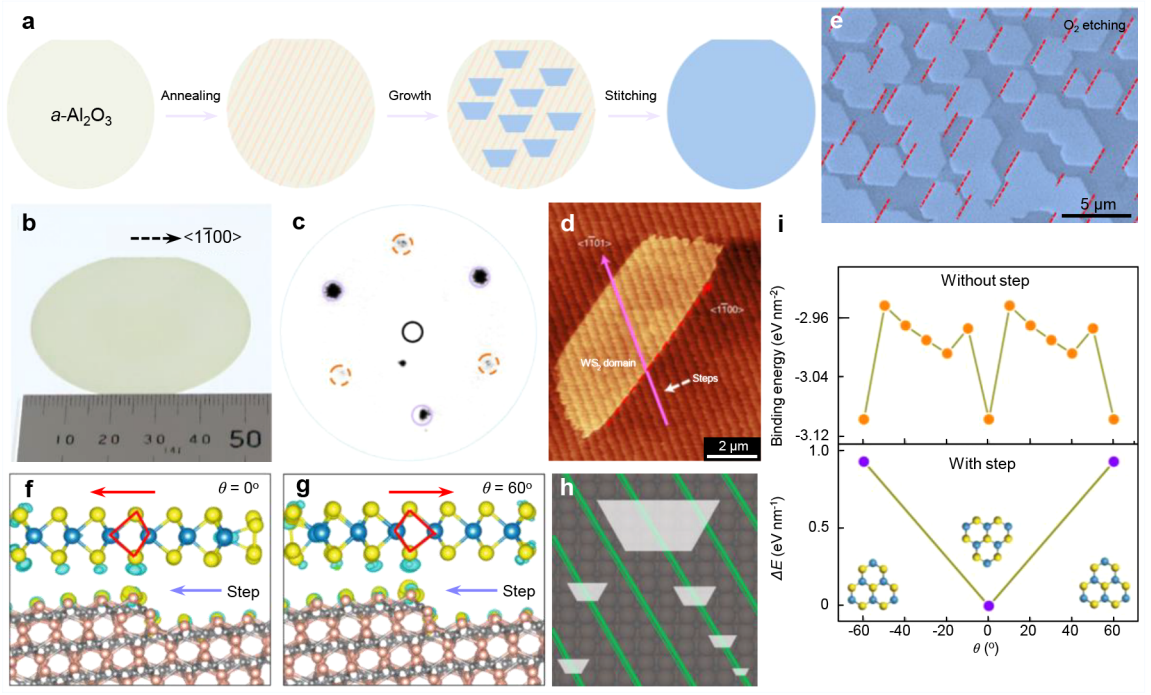

Figure 13. (a) The growth process of single-crystal WS_2 films on a-Al_2O_3. (b) A photograph of WS_2/a-Al_2O_3. (c) Representative LEED pattern of the WS_2 film. (d) AFM image of a WS_2 island. (e) False-color SEM image of WS_2 films after O_2 etching. (f,g) Optimized structures of antiparallel WS_2 on a-Al_2O_3. (h) Schematic of WS_2 islands grown on a-Al_2O_3 during the early stage of growth. (i) Theoretical analysis and DFT calculation of WS_2 epitaxial growth with and without steps. (Reproduced from ref 61. Copyright 2022 Springer Nature).

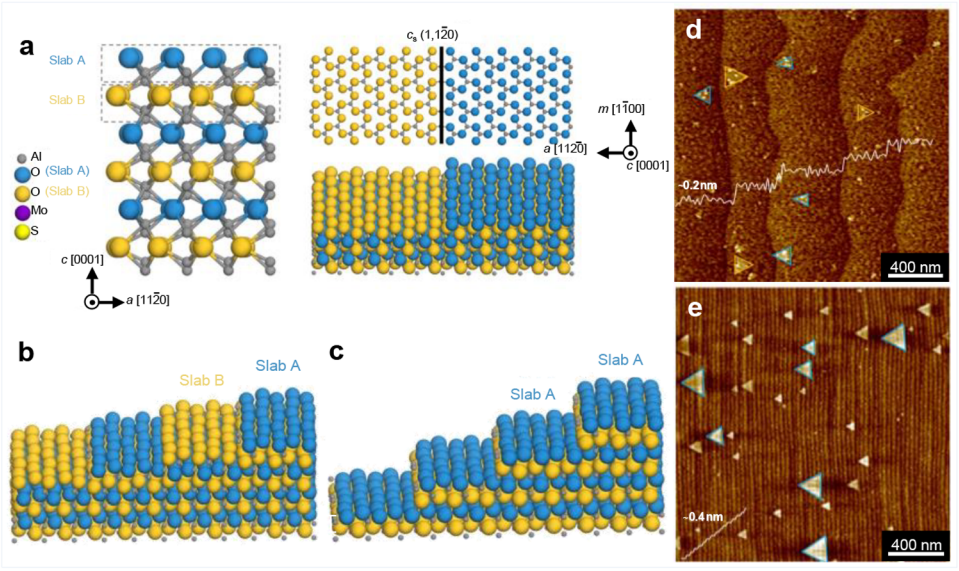

Figure 14. (a−c) Schematic diagrams of sapphire surface with 3-fold atomic arrangement. (d,e) AFM images of antiparallel and unidirectional aligned MoS_2 islands. (Reproduced from ref 55. Copyright 2023 Springer Nature).

4.2. Growth of Single-Crystal TMDs from Multiple Nuclei

Currently, the size of monolayer TMDs single crystal prepared from one nucleus can reach millimeters, but it is still far away from the required wafer-scale single crystals. Then, the epitaxy growth from multiple nuclei was introduced. This method need a lattice-matched substrate for the epitaxy of TMD islands with uniform directions, followed by their coalescence into single crystals.[133]

4.2.1. Steps-Guided Epitaxial Growth. It has been demonstrated that single-crystal hBN can be obtained on vicinal Cu (110) substrates with parallel steps.[56] Similarly, Yang et al. reported the epitaxy of monolayer MoS_2 single crystals on vicinal Au (111) surface (Figure 12a,b).[60] STM characterizations and first-principles calculations reveal that the nucleation of MoS_2 is generally occurred on Au steps, leading to unidirectional MoS_2 islands along the step edges and finally stitched to a continuous film (Figure 12c−e). In addition, it was found that the formation of 60°-oriented islands can be inhibited by precisely regulating the S/Mo ratio. Overall, this work presents a direct approach for

https://doi.org/10.1021/prechem.3c00122
Precis. Chem. 2024, 2, 330−354

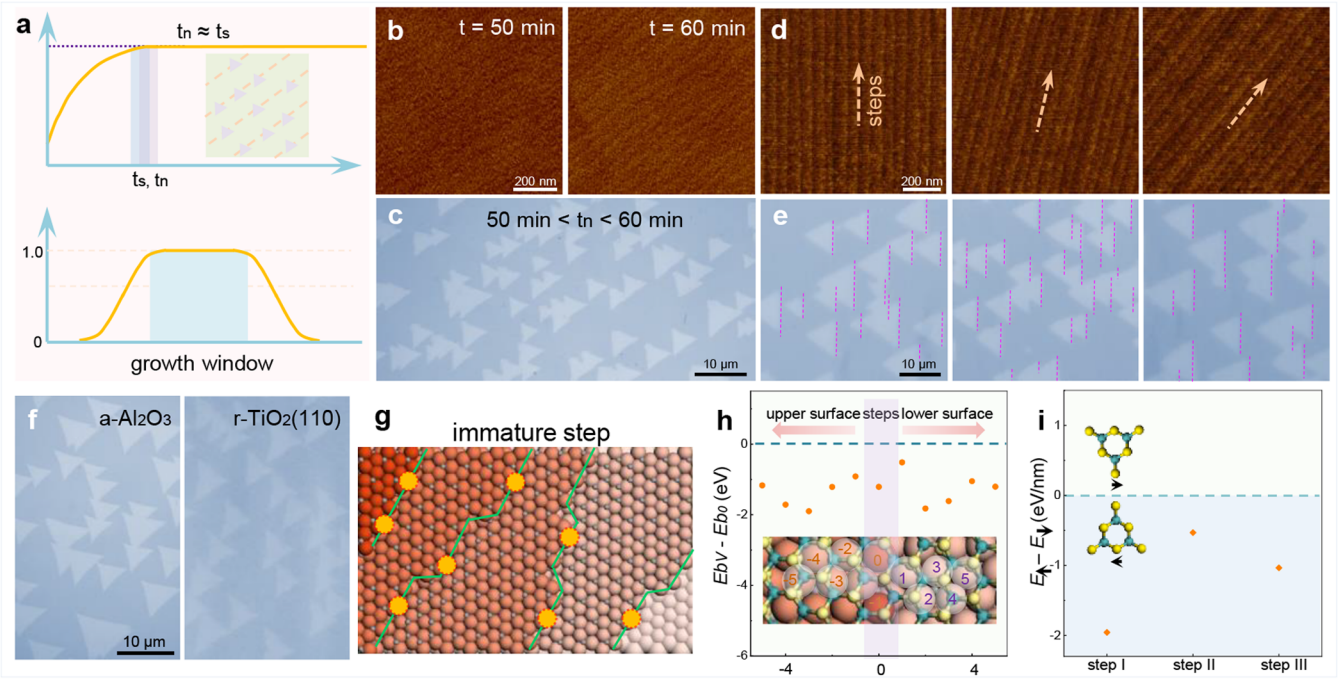

Figure 15. (a) Schematic illustration of the growth process of MoS_2. (b) AFM images of vicinal c-Al_2O_3 surfaces annealed at different times. (c) Optical images of MoS_2 grains on c-Al_2O_3 at 50−60 min. (d) AFM images of the c-Al_2O_3 surface. (e) Optical images of MoS_2 grains on c-Al_2O_3 substrates. (f) Optical images of MoS_2 grains on a-Al_2O_3 and r-TiO_2 (110) substrates. (g) Schematic diagrams of the c-Al_2O_3 surface during annealing at high temperature. (h) The binding energy difference of a MoS_2 grain on a step without/with O vacancy. (i) Energy difference between two antiparallel MoS_2 grains across different steps. (Reproduced from ref 53. Copyright 2023 Springer Nature).

synthesizing centimeter-scale TMD single crystals on metal substrates.

Considering the practical applications of TMDs films, achieving direct synthesis on insulating substrates is the ultimate goal. Sapphire has been extensively employed as an epitaxial substrate.[134] Li et al. designed a cross-cut direction toward the sapphire's A-axis to prepare a 2-in. monolayer MoS_2 single crystal (Figure 12f,g).[54]

4.2.2. Dual-Coupling-Guided Epitaxial Growth. Step-guided growth of noncentrosymmetric 2D materials needs strong couplings between the 2D materials and step edges to guarantee the unidirectional alignment. However, for the insulating sapphire substrates, such strong edge-step coupling may not be feasible. Therefore, the epitaxy mechanism of 2D TMDs on insulating substrates may be significantly different from that on metal substrates. Wang et al. have proposed some guidelines for selecting a suitable insulating substrate.[61] Vicinal a-plane sapphire (a-Al_2O_3) was first annealed at high temperatures in an O_2 atmosphere to stabilize the parallel atomic steps. These atomic step edges were intentionally engineered to break the C_2 symmetry and direct the aligned growth of WS_2 islands (Figure 13a). Then, a 2-in.-sized single-crystal WS_2 monolayer was successfully synthesized (Figure 13b). LEED, second-harmonic generation (SHG) and O_2 etching evaluations confirmed that the film was formed by unidirectionally aligned WS_2 islands (Figure 13c and e). High-resolution AFM images of WS_2 islands further confirmed existence of parallel steps, along with the lattice orientation of WS_2 and sapphire (Figure 13d). Based on theoretical analysis and DFT calculations, the authors discovered that the epitaxy of WS_2 on a-Al_2O_3 surface is governed by a dual-coupling-guided mechanism. (Figure 13f−i).

4.2.3. Surface-Reconstruction-Guided Epitaxial Growth. The prevailing view is that the alignment of 2D TMDs grain is primarily driven by step-edge-guided epitaxy. However, Fu et al. have indicated that the interaction of 2D TMDs grains and exposed O−Al atomic planes can also play a significant role in achieving the unidirectional alignment.[55] This interaction leads to a minimized energy structure of 2D TMDs grains on c-Al_2O_3 regardless of the cutoff tilt angle (Figure 14a−c). When the type of steps is alternating slabs of A and B, the orientation of the MoS_2 nucleus growing on two neighboring steps is antiparallel (Figure 14d). In contrast, unidirectional growth of MoS_2 can be achieved when a single type of step is formed over the entire surface of the sapphire substrate (Figure 14e). The cross-sectional transmission electron microscopy (TEM) image confirms that the step height is ∼0.4 nm, and the monolayer MoS_2 grows seamlessly along the a/a terrace. Therefore, the preparation of the appropriate atomic surface structure is also important to the growth of single crystals.

4.2.4. Simultaneous Formation of Grain Nuclei and Substrate Steps. Although unidirectionally aligned TMDs have been achieved by many groups, the antiparallel islands during epitaxial growth were reported by more works, even on the same substrate.[135−153] Currently, experimental window for epitaxial growth of noncentrosymmetric 2D materials is very narrow, and the key mechanism for ensuring such epitaxy remains unclear. In 2023, Zheng et al. highlighted that the time of TMDs nucleation (t_n) and the substrate steps formation (t_s) is critical for single-crystal growth.[53] When $t_n \approx t_s$, immature step edges become active sites for 2D grain nucleation, ensuring unidirectional alignment in a broad growth window (Figure 15a). AFM images reveal the parallel steps after annealing for ∼200 min (Figure 15b). Unidirectionally aligned MoS_2 grains are easily achieved on c-Al_2O_3 substrate when $t_n \approx t_s$ (Figure 15c). Notably, among the nine tested step orientations, all grown MoS_2 grains aligned along the same direction of the c-

https://doi.org/10.1021/prechem.3c00122
Precis. Chem. 2024, 2, 330−354

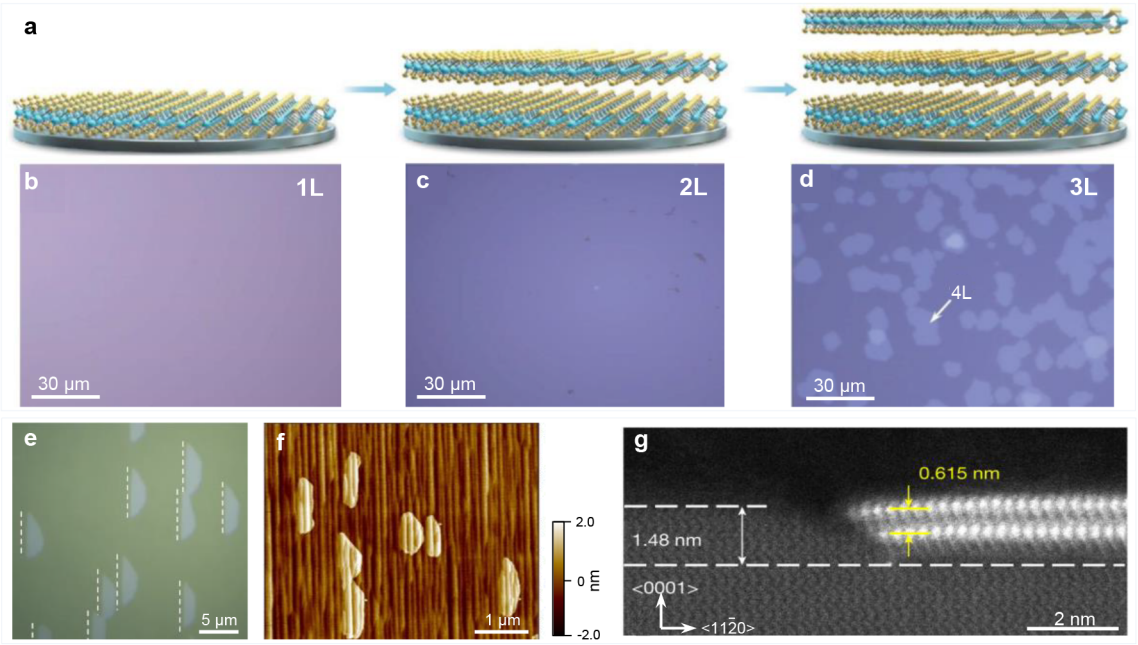

Figure 16. (a) Schematic diagrams of epitaxy growth. (b–d) Optical images of MoS_2 with different layer. (Reproduced from ref 156. Copyright 2022 Oxford University Press). (e) Optical image and (f) AFM image of bilayer MoS_2 islands. (g) Cross-sectional STEM image of bilayer MoS_2. (Reproduced from ref 157. Copyright 2022 Springer Nature).

Al_2O_3 surface (Figure 15d,e). This technique is also applicable to other substrates (Figure 15f). The epitaxy can extend to other TMDs like WS_2, NbS_2, $MoSe_2$, WSe_2, and $NbSe_2$. DFT results provide insights into the mechanism of the universal epitaxy. During annealing, most oxygen vacancies disappeared, except for those near steps (Figure 15g). The negative value of the binding energy of a MoS_2 grain on a step without/with O vacancy ($E_{bV} - E_{b0}$) suggests stronger interaction of MoS_2 grains with defective steps (Figure 15h). Then antiparallel MoS_2 grains can be effectively distinguished (Figure 15i).

4.3. Growth of Bilayer and Multilayer TMDs

To date, a wide range of high-quality monolayer TMDs chips have been successfully fabricated, ranging from individual transistors to integrated circuits. Compared to the monolayer TMDs, the multilayer ones exhibit a narrow band gap with enhanced carrier mobility and photon absorption ability.[154,155] However, achieving uniform high-quality multilayer TMDs single crystals remains an ongoing challenge. The main challenges for the growth of bilayer/multilayer TMDs single crystals are as follows: (i) Bilayer/multilayer TMDs have a higher nucleation barrier compared to monolayers, making it more preferable to grow monolayers on most substrates. (ii) The strong vdW interaction between the substrate and epitaxial TMDs makes it challenging to obtain uniform bilayer/multilayer films, with upper layer growth being more difficult than the lower layer.

To produce uniform TMDs bilayers, two approaches can be chosen, namely layer-by-layer growth and edge-guided bilayer nucleation and growth. In 2022, Wang et al. grew 4-in. high-quality multilayer MoS_2 wafers with a controlled number of layers (Figure 16a).[156] First, they used oxygen-assisted CVD to break the self-limiting growth of MoS_2 monolayers and reduce the reaction energy barriers during the growth process. Second, they elevated the temperature of the MoO_3 and substrate to increase the nucleation density and edge growth rate of the second layer. Finally, uniform NL-MoS_2 (N = 1, 2, 3) growth was successfully achieved in a layer-by-layer manner with epitaxy process repeated, where N is the layer number (Figure 16b–d). During the same period, Liu et al. reported the uniform bilayer MoS_2 on c-Al_2O_3 using the bilayer nucleation strategy.[157] The height of the steps is designed to realize the edge nucleation and MoS_2 island coalescence into continuous centimeter-level films (Figure 16e–g). They achieved a six-step terrace matching the height of bilayer MoS_2 by annealing the c-Al_2O_3 at high temperature. Meanwhile, they increased the concentration of precursors to ensure the formation and growth of bilayer nuclei.

4.4. Growth of Stacking-Controlled TMDs

When putting 2D monolayers together, the weak vdW coupling allows for various interlayer stacking configurations. Taking TMDs as an example, the monolayers will rotate 60° to each other to form the centrosymmetric hexagonal stacking structure (2H) or parallelly stack with the same direction to obtain the noncentrosymmetric rhombohedral stacking sequence (3R).[158]

Previously, Zhang et al. achieved a series of large-sized TMDs bilayers with different stacking through the reverse-flow chemical vapor epitaxy.[159] They first grew the monolayer TMDs on the substrate at a lower temperature (700 °C), then increased the temperature to make the vertical epitaxial growth of the second monolayer more easily than the lateral epitaxy. At the preferred growth temperature, 3R- and 2H-TMDs bilayers were successfully obtained. While the universal growth of the large-scale single-crystal pure-phase 3R-TMDs multilayer films remains a great challenge but urgent need for development due to their higher mobility,[158] stronger optical nonlinearity,[160,161] interlayer ferroelectricity, etc.[162,163]

4.5. Growth of Twist-Controlled TMDs

Besides the commensurate stacking configuration with the interlayer angles of both 0° and 60°, the twistedly stacked 2D multilayers have attracted widespread interest in the past few years. In 2014, Liu et al. grew the bilayer MoS_2 islands with various twist angles by a regular CVD method (Figure 17a) and

https://doi.org/10.1021/prechem.3c00122
Precis. Chem. 2024, 2, 330–354

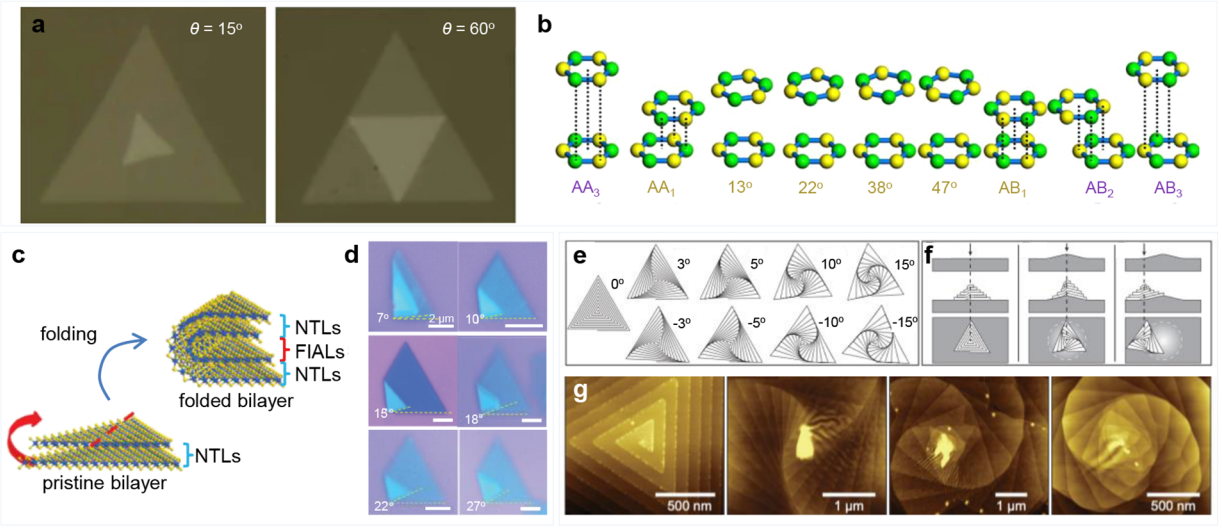

Figure 17. (a) Optical images of twisted bilayers MoS_2. (b) Schematics of MoS_2 bilayers different twisted angles. (Reproduced from ref 164. Copyright 2014 Springer Nature). (c) The illustration of the folding process. (d) Optical microscopy images of folded bilayer MoS_2 with different twist angles. (Reproduced from ref 169. Copyright 2022 Wiley). (e) Simulated superstructures of triangular dislocation spiral. (f) Aligned spirals, fastened supertwisted spiral and unfastened supertwisted spiral. (g) AFM images of aligned WS_2 spirals and representative WS_2 supertwisted spirals with various twist angles. (Reproduced from ref 172. Copyright 2020 American Association for the Advancement of Science).

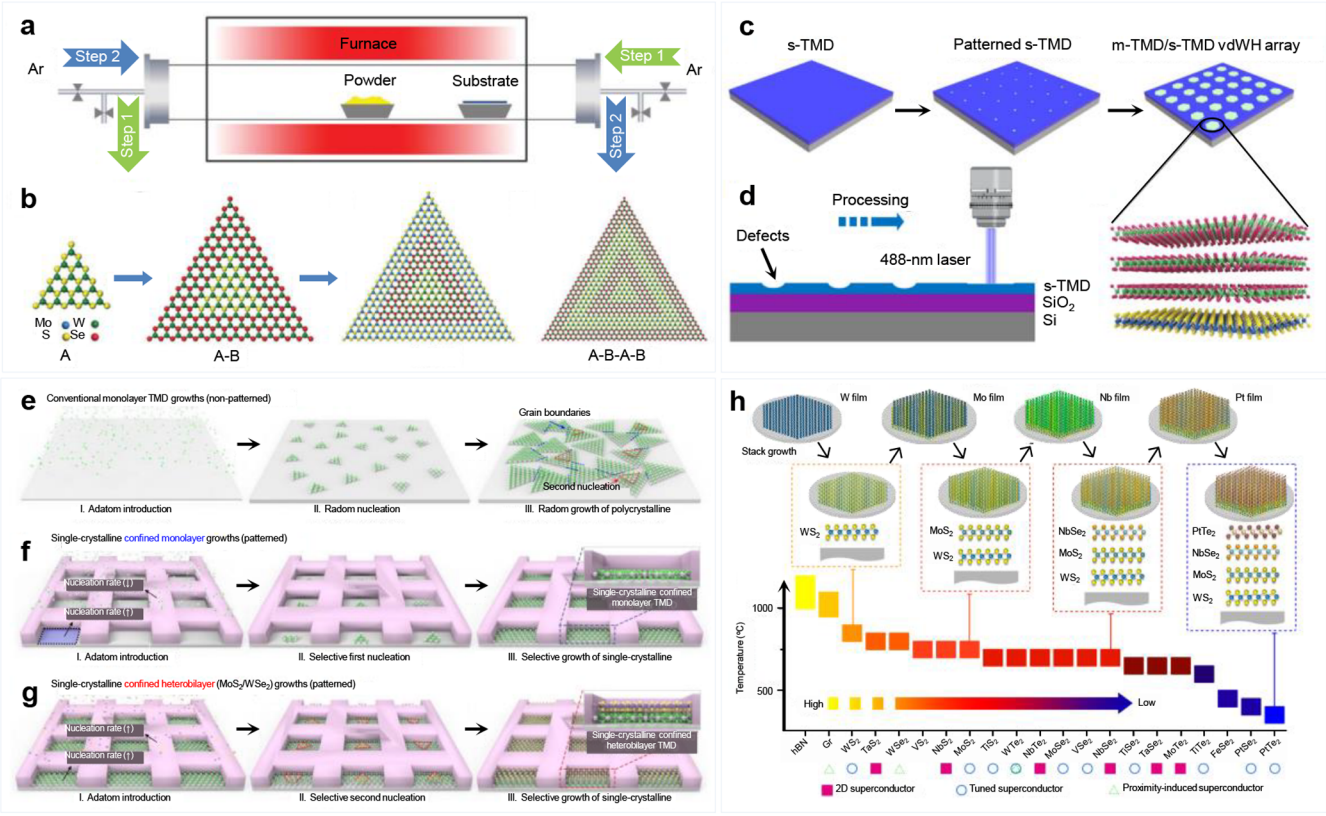

Figure 18. (a) Schematic diagrams of the CVD system. (b) 2D monolayer seed, and heterostructures. (Reproduced from ref 173. Copyright 2017 American Association for the Advancement of Science). (c) Schematic diagrams of the growth process of TMDs. (d) Schematic diagram of the laser-patterning process. (Reproduced from ref 176. Copyright 2020 Springer Nature). (e) Schematic of the general process by which TMDs are grown. (f) Schematic of the selective single-island synthesis strategy. (g) Single-island MoS_2/WSe_2 heterostructures by confined growth of a second MoS_2 layer. (Reproduced from ref 177. Copyright 2023 Springer Nature). (h) Stacking growth of vdW superconductor heterostructures guided by the high-to-low temperature strategy. (Reproduced from ref 178. Copyright 2023 Springer Nature).

found that the incommensurate stacking order would enlarge the separations between two MoS_2 monolayers, resulting in the reduction of the interlayer coupling (Figure 17b).[164] The centimeter-scale bilayer MoS_2 homostructures with the precise control of interlayer twist angle (accuracy of ~2°) were realized by growing monolayer MoS_2 combined with a water-assisted

https://doi.org/10.1021/prechem.3c00122
Precis. Chem. 2024, 2, 330−354

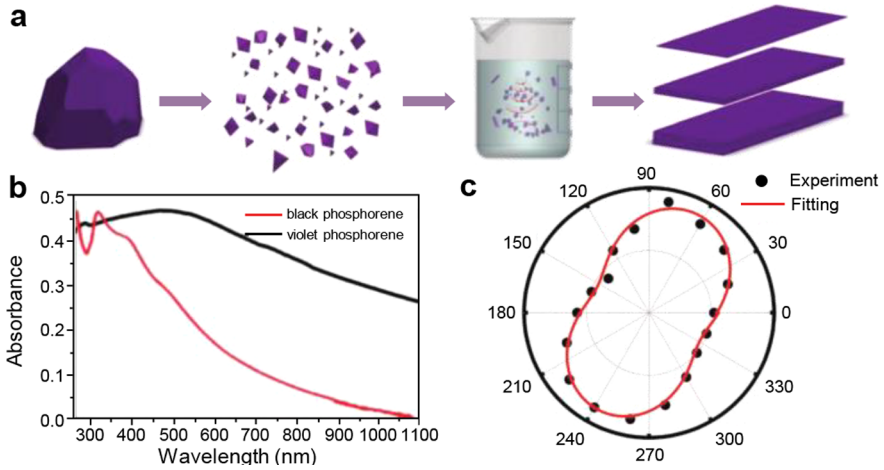

Figure 19. (a) The preparation processes, (b) UV−vis−NIR absorption spectrum of violet phosphorene. (c) The angle-dependent SHG polarization pattern. (Reproduced from ref 185. Copyright 2023 Wiley).

clean transfer method.[165] Recently, a method to grow large twist bilayer graphene (TBG) with controlled angles was explored.[166] In detail, the twist angle of TBG was docked by the two prerotated Cu (111) substrates to form a Cu/TBG/Cu sandwich structure, and then an equipotential surface etching process was applied to isolate the TBG film. Such growth technique may be extended to achieve the large-sized growth of twist bilayer TMDs with the more precisely controlled twist angle.

The fabrication of twist-stacked 2D multilayers has also made some progress. Traditionally, the twisted multilayer superlattices are obtained by artificially stacking the selected flakes.[167,168] Zhang et al. realized the twisted MoS_2 multilayers by the paraffin-assisted folding of nontwisted ones (Figure 17c).[169] The twist angle could be well controlled ranging from around 3° to 27° (Figure 17d). For creating the high-order twisted superlattice with multiple twisted interfaces, also named spiral or screw structure, the CVD growth technique is a widely used route.[170,171] Figure 17e showed the shapes of a range of twisted superstructures.[172] Through the geometric and mathematical analysis, the growth behavior of twisted multilayer was found to be extremely dependent on the morphology of the substrate surface, e.g., an unfastened supertwisted spiral would be grown on a protruded substrate (Figure 17f). Finally, such supertwisted spirals of WS_2 and WSe_2 were successfully grown on the non-Euclidean surface of SiO_2/Si substrates (Figure 17g).

4.6. Growth of TMD Heterostructures

All above-mentioned TMDs are of the homostructures, and combining them together as heterostructures in either lateral or vertical directions will bring novel properties and potential applications. Various approaches have been employed to synthesize these fashionable and functional heterostructures.

The in-plane heterostructures were generally obtained by the epitaxy of the subsequent components at the edge of the existing 2D materials. In 2017, Zhang et al. reported a reverse-flow synthetic strategy (Figure 18a),[173] where the substrate-to-source or source-to-substrate flow was alternatively applied to prevent undesired thermal degradation of the as-grown 2D crystals (step 1) or transport the growth sources for the epitaxy of the target ones (step 2), to obtain the various lateral heterostructures and even superlattices (Figure 18b). Subsequently, a one-pot growth method was proposed to synthesize the multiheterojunctions by the precise modulation of gas with water vapor, which would help the oxidation, volatilization, and nucleation of the transition-metal sources, and sequential edge epitaxy of the TMDs monolayers.[174] Furthermore, the arrayed heterostructure monolayer films were realized by using the specific laser patterning and thermal etching process on the existing monolayer and following the epitaxial growth of another 2D crystal.[175] These works with sharp interfaces have built up a rationally designed platform for the further development of integrated 2D lateral heterostructures based on the mature growth technique of large-scale single-crystal monolayers.

The vertical heterostructures can be fabricated by artificially stacking the vdW 2D materials via a polymer-assisted dry-transfer method. The direct heteroepitaxy, possessing better contact and a cleaner interface without the resident dopants, is expected to be scalable for practical applications. As shown in Figure 18c, the nucleation and vertical epitaxy of various metallic TMDs enabled to be precisely controlled by the selectively patterned nucleation sites on the existing monolayer or bilayer semiconducting TMDs through the focused laser irradiation (Figure 18d).[176] In the meanwhile, Kim et al. proposed a geometric-confinement growth technique to obtain large-area 2D monolayer arrays and their heterostructures on various substrates.[177] The traditional CVD growth of monolayer TMDs films would generally involve the random nucleation and the formation of grain boundaries (Figure 18e). In contrast, they selectively constructed the growth areas via patterning SiO_2 masks to confine the monolayer or heterostructures only growing into these areas rapidly from the single nucleus to eventually form the single islands (Figure 18f,g). Recently, wafer-scale multiple-layered heterostructures, ranging from double- to five-block layers, have been realized via a high-to-low temperature growth strategy in the two-step vapor-deposition system.[178] This success mainly relied on the relatively lower growth temperature of the subsequent component than that of the existing one (Figure 18h). The well designed interfaces with very little contamination between the adjacent layers was also demonstrated by the detailed characterizations. Based on these works, the rationally designed synthesis of single-crystal multilayer heterostructures with tunable components and atomically sharp interfaces on a large scale is highly desired.

https://doi.org/10.1021/prechem.3c00122
Precis. Chem. 2024, 2, 330−354

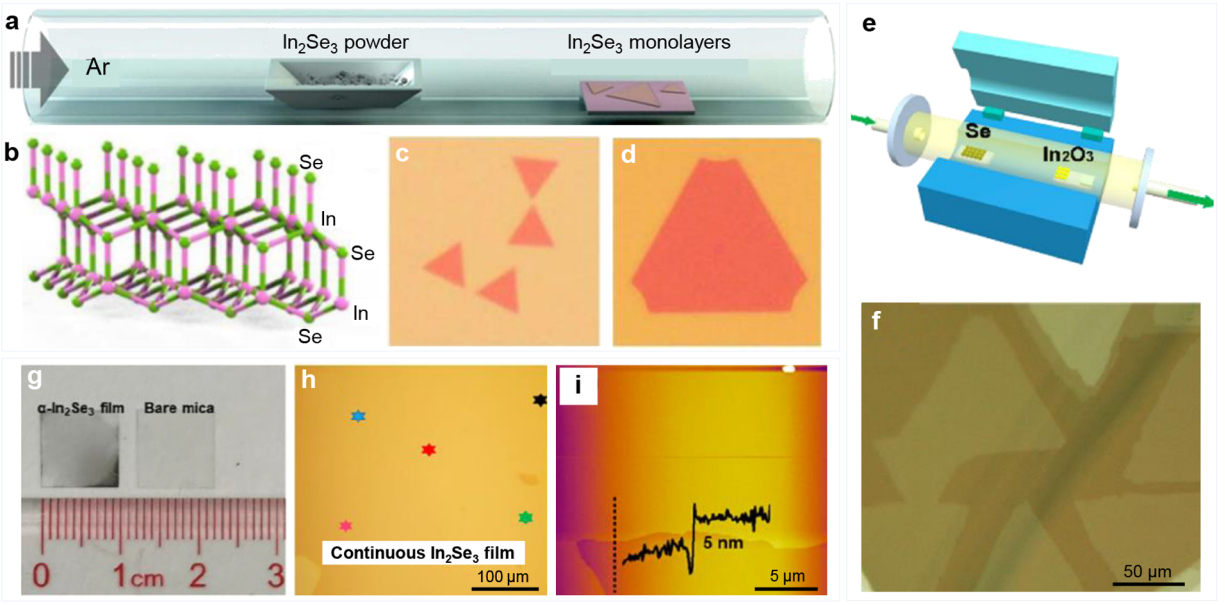

Figure 20. (a,b) PVD growth process and crystal structure of monolayer In_2Se_3. (Reproduced from ref 192. Copyright 2015 American Chemical Society). (c,d) Optical images of In_2Se_3. (e,f) Schematic diagram of the CVD setup and optical image of 2D In_2Se_3. (Reproduced from ref 193. Copyright 2016 American Chemical Society). (g) Photograph of the bare mica substrate and the In_2Se_3 film. (h) Optical image of the In_2Se_3 film. (i) AFM image of the In_2Se_3 film. (Reproduced from ref 194. Copyright 2023 American Chemical Society).

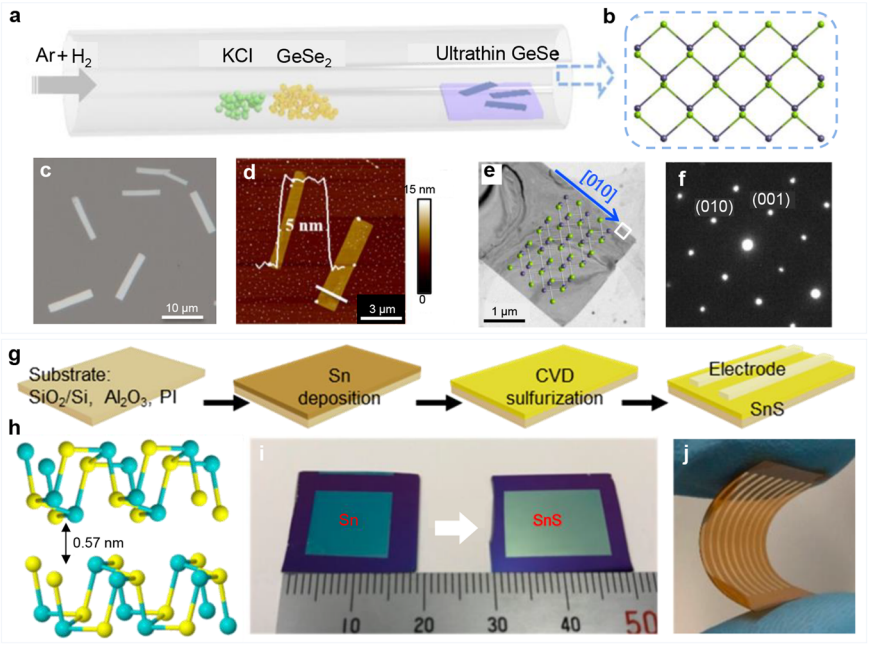

Figure 21. (a) Schematic diagram of the setup. (b) Structure of layered GeSe. (c,d) Optical and AFM images of synthesized GeSe. (e,f) Low-magnification TEM image and electron diffraction pattern of a GeSe flake. (Reproduced from ref 205. Copyright 2019 American Chemical Society). (g) Procedures for the growth of SnS. (h) Structure of orthorhombic 2D SnS layers. (i) Patternable and scalable growth of 2D SnS layers. (j) Flexible 2D SnS layers grown on PI substrates. (Reproduced from ref 206. Copyright 2023 American Chemical Society).

5. GROWTH OF OTHER NONCENTROSYMMETRIC 2D MATERIALS

5.1. Growth of 2D Elemental Materials

Besides graphene, other 2D elemental materials such as phosphene (black phosphorus, BP), silicene, germanene, and tellurene have also attracted substantial attention owing to their notable properties, including high carrier mobility, strong in-plane anisotropy, and adjustable bandgap.[179−183] Most of these 2D elemental materials are centrosymmetric. However, in 2020, Zhang et al. successfully synthesized noncentrosymmetric violet phosphorus single crystals, providing the first reliable lattice structure.[184] Subsequently, Ma et al. achieved the exfoliation of violet phosphene through sonication in ethanol (Figure 19a).[185] The crystal structure of violet phosphine exhibits lower symmetry due to its vertically stacked interlocking cross-chain arrangement. The ultraviolet−visible−near−infrared (UV−vis−NIR) absorption spectra demonstrate the enhanced light

https://doi.org/10.1021/prechem.3c00122
Precis. Chem. 2024, 2, 330−354

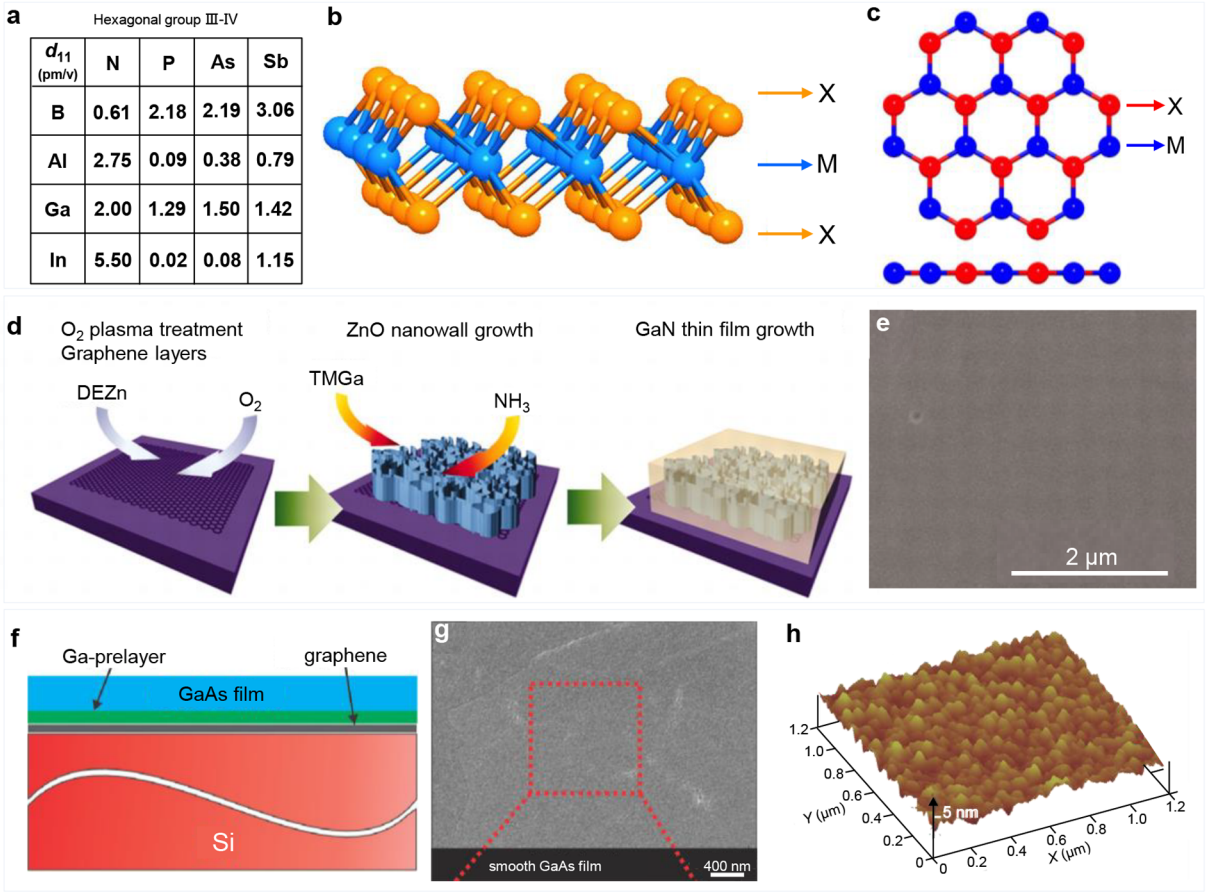

Figure 22. (a) Periodic trends for d_{11} in group III−V semiconductors. (b,c) 2H and planar hexagonal structures of group III−V semiconductors. (Reproduced from ref 207. Copyright 2015 American Chemical Society). (d) Schematic diagrams of epitaxial growth of GaN thin films. (e) GaN thin film grown on ZnO nanowalls. (Reproduced from ref 212. Copyright 2010 American Association for the Advancement of Science). (f) Schematic diagram of cross-section view of the GaAs films/Ga-prelayer/graphene/Si. (g) SEM plan-view image and (h) AFM image of ultrasmooth GaAs films. (Reproduced from ref 213. Copyright 2014 Wiley).

absorption of violet phosphene in the visible and infrared regions compared to BP (Figure 19b). Polarization measurements of violet phosphine reveal varying SHG responses dependent on the polarization angles, consistent with the 2-fold rotational symmetry of its crystal structure (Figure 19c).

5.2. Growth of 2D Group III Monochalcogenides

Among the group III monochalcogenides, In_2Se_3 stands out as a captivating 2D ferroelectric material because of its intrinsic properties of direct band gap (1.36 eV), multiphase, and in-plane and out-of-plane polarizations. These distinctive properties make it highly suitable for the applications such as electromechanical transducers, phase-change memories, optoelectronics, and photovoltaics.[186−191]

In 2015, Zhou et al. employed physical vapor deposition to produce a high-quality α-In_2Se_3 monolayer (Figure 20a).[192] The α-In_2Se_3 monolayer consists of a quintuple layer with vertically aligned "Se−In−Se−In−Se" with "Se−In−Se" stacking on one side and "Se−In" stacking on the other (Figure 20b). Different growth times can obtain triangular In_2Se_3 monolayers and multilayers (Figure 20c,d). Then, Feng et al. successfully achieved the epitaxial growth of large-scale 2D In_2Se_3 nanosheets with a lateral size of ∼100 μm on a mica substrate (Figure 20e,f).[193] More recently, He et al. demonstrated the growth of larger-area In_2Se_3 films via selenylation of In_2O_3 using the CVD method.[194] Notably, the size of continuous In_2Se_3 films grown on a mica substrate can reach 1 × 1 cm^2 (Figure 20g−i).

5.3. Growth of 2D Group IV Monochalcogenides

Group IV monochalcogenides (MXs, where M = Sn or Ge and X = S or Se) have attracted substantial attention due to their unique orthorhombic structure, eco-friendly nature, resource abundance, and cost-effectiveness.[195−199] Especially, their vdW structure can yield significant in-plane piezoelectric properties and pronounced anisotropy.[200] These properties make them promising candidates for broad-scale utilization in photovoltaic and thermoelectric applications.[201−203]

Synthesizing ultrathin GeSe is very challenging due to the strong interlayer forces and complex phases.[204] Taking inspiration from the successful growth of 2D TMDs using the molten salt-assisted CVD method, Hu et al. employed a similar approach to produce ultrathin 2D α-GeSe flakes (Figure 21a,b).[205] Ultrathin 2D α-GeSe flakes grown on mica substrates exhibit dimensions of 3 μm in width and 15 μm in length with a minimal thickness of 5 nm (Figure 21c−f). To ensure compatibility in the output and fabrication of piezoelectric devices based on MXs with inherent piezoelectric properties, Yoo et al. conducted the synthesis of centimeter-scale 2D SnS layers on various substrates via vulcanization of predeposited Sn film (Figure 21g,h).[206] The scalability of this growth method is demonstrated by successful production of 2D SnS films

https://doi.org/10.1021/prechem.3c00122
Precis. Chem. 2024, 2, 330−354

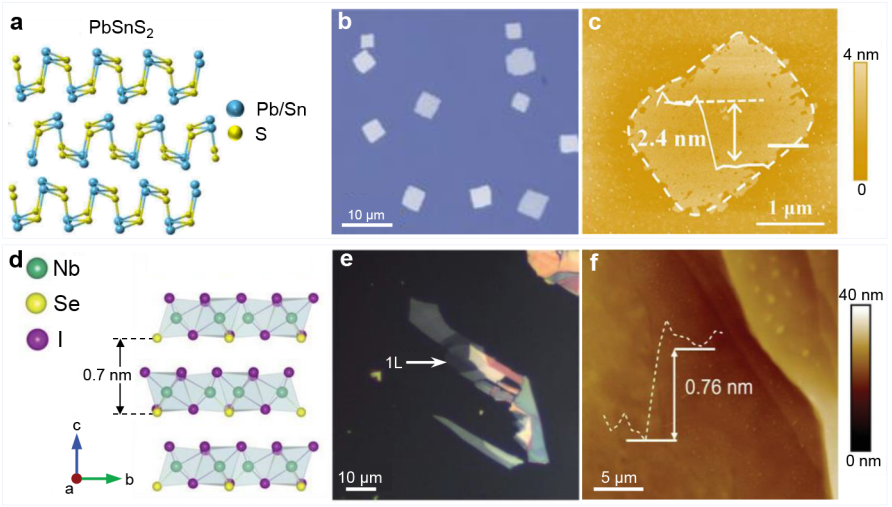

Figure 23. (a) The atomic structure of $PbSnS_2$. (b) Optical image of $PbSnS_2$ nanoplates. (c) AFM image of a $PbSnS_2$ flake. (Reproduced from ref 218. Copyright 2020 Elsevier). (d) Crystal structure of Nb_3SeI_7. (e) Bright-field optical images of Nb_3SeI_7 with varied thicknesses. (f) AFM image of monolayer Nb_3SeI_7. (Reproduced from ref 219. Copyright 2023 Wiley).

exceeding 1.5 cm^2 (Figure 21i). Notably, the growth temperature is as low as 200 °C, which is tolerable for a wide range of polymer substrates. This enables the direct growth of SnS on polyamides (PIs, 50 μm) substrates with integrated gold electrodes while maintaining excellent mechanical properties (Figure 21j).

5.4. Growth of 2D Group III−IV Binary Compounds

Some 2D group III−IV binary compounds break the inversion symmetry of the crystal structure, thereby exhibiting piezoelectricity and demonstrating an in-plane piezoelectric coefficient (Figure 22a−c).[207] In addition, GaN and GaAs offer numerous advantages for optoelectronic device applications due to their high carrier mobility and long-term stability.[208−211] Chung et al. successfully grew GaN films on graphene layers utilizing densely aligned ZnO nanowalls as an intermediary substrate (Figure 22d).[212] The initial step involved plasma oxygen treatment of the graphene, creating distinct stepped edges. Subsequently, high-density ZnO nanowalls were grown on the graphene substrate. Given the minimal lattice mismatches between ZnO nanowalls and GaN, it became possible to achieve lateral epitaxy for GaN films on these nanowalls (Figure 22e). In 2014, Alaskar et al. demonstrated the first growth of ultrasmooth GaAs films on graphene/silicon substrates using quasi-vdW epitaxy.[213] The employment of Ga-prelayers could produce a smooth surface (Figure 22f). Besides the impact of the Ga coating, the lower growth rate is also helpful for the smooth GaAs surface (Figure 22g,h).

5.5. Growth of 2D Ternary Compounds

Beyond 2D binary materials, the presence of variable stoichiometry in 2D ternary materials provides additional degrees of freedom.[214−217] Shu et al. have introduced a novel CVD method for synthesizing ultrathin $PbSnS_2$ flakes using salt (KCl) and molecular sieves ($Na_{12}[(AlO_2)_{12}(SiO_2)_{12}]$-$xH_2O$, where x denotes the water crystals number).[218] This method effectively lowers the metal precursor's melting point by adsorbing and trapping evaporated molecules, ensuring a uniform distribution of the source (Figure 23a−c). More recently, Wang et al. reported the synthesis of Nb_3SeI_7, a new ternary layered material via chemical vapor transport (CVT).[219] Nb_3SeI_7 possesses a noncentrosymmetric lattice structure and exhibits pronounced SHG, in-plane anisotropic electrical properties, and optical absorption capabilities (Figure 23d−f).

Overall, most of the current works on the production of noncentrosymmetric 2D single crystals are focused on the hBN and TMDs. For the noncentrosymmetric 2D materials mentioned in this section, including 2D elemental materials, 2D group III monochalcogenides, 2D group IV monochalcogenides, 2D group III−IV binary compounds, and 2D ternary compounds, there remains ample scope for advancements in the synthesis of their single crystals. Presently employed methods only yield a limited number of individual islands or polycrystalline films. The control over nucleation density and lattice orientation in these materials is still at an early stage with scarce reports available. Therefore, further exploration and research are imperative for future investigations.

6. CONCLUSION AND PERSPECTIVE

In conclusion, the precise preparation techniques of single nucleus control and multiple nuclei collaboration for wafer-scale single-crystal noncentrosymmetric 2D materials, especially monolayer films, have significantly advanced for their high-end applications. This review provides a comprehensive summary of the recent advancements achieved in this field. However, to successfully integrate 2D materials into real production processes, several requirements must be met. These include achieving extreme uniformity and repeatability of crystal quality,[220] ensuring all-component growth or ultraclean transfer on Si-based wafers,[221−223] implementing low-temperature single-crystal preparation,[224,225] as well as attaining controllable dopant distributions and doping levels.[226,227]

In the meantime, multilayer noncentrosymmetric 2D materials with higher device performance (including mobility, on−off ratio, and electrostatic control),[228,229] lower integration threshold,[230] and novel physical properties (strong-correlated states, sliding ferroelectricity, moiré excitons, etc.),[231−234] have been highly desired. However, both R- and H-stacked 2D materials exhibit similar formation energies, resulting in uncontrolled stacking structures and unavoidable grain boundaries. The epitaxial growth of 2D heterostructures also encounters this issue, as different configurations possess

https://doi.org/10.1021/prechem.3c00122
Precis. Chem. 2024, 2, 330−354

comparable energies. Similar to the growth of monolayer noncentrosymmetric 2D single crystals, this energy degeneracy may also be addressed by introducing steps, but certainly requires more precise control.

In terms of twist angle, the continuous twisting of superlattices has been limited to the single-island scale due to thermodynamic instability. This thermodynamic instability may be solved by introducing additional degrees of freedom. For instance, a seed crystal with adjustable angle can be placed on the first layer of material to achieve epitaxial growth of angle-controlled 2D materials.

In conclusion, significant advancements have been achieved in the production of monolayer single-layer 2D materials thus far, leading to the development of integrated devices that exhibit exceptional performance. The number of layers, twist angle, and stacking configurations can offer novel opportunities for controlling the physical properties of 2D materials, and the consequent revolutionary applications. Therefore, the production of 2D single crystals will continue to be a crucial research focus in the forthcoming decade.

AUTHOR INFORMATION

Corresponding Authors

Xiaozhi Xu − *Guangdong Basic Research Center of Excellence for Structure and Fundamental Interactions of Matter, Guangdong Provincial Key Laboratory of Quantum Engineering and Quantum Materials, School of Physics, South China Normal University, Guangzhou 510631, China; Guangdong−Hong Kong Joint Laboratory of Quantum Matter, Frontier Research Institute for Physics, South China Normal University, Guangzhou 510631, China;* orcid.org/0000-0003-1067-9590; Email: xiaozhixu@scnu.edu.cn

Kaihui Liu − *State Key Laboratory for Mesoscopic Physics, Frontiers Science Center for Nano-optoelectronics, School of Physics, Peking University, Beijing 100871, China; Songshan Lake Materials Laboratory, Institute of Physics, Chinese Academy of Sciences, Dongguan 523820, China;* orcid.org/0000-0002-8781-2495; Email: khliu@pku.edu.cn

Authors

Guoliang Cui − *Guangdong Basic Research Center of Excellence for Structure and Fundamental Interactions of Matter, Guangdong Provincial Key Laboratory of Quantum Engineering and Quantum Materials, School of Physics, South China Normal University, Guangzhou 510631, China; Guangdong−Hong Kong Joint Laboratory of Quantum Matter, Frontier Research Institute for Physics, South China Normal University, Guangzhou 510631, China*

Jiajie Qi − *State Key Laboratory for Mesoscopic Physics, Frontiers Science Center for Nano-optoelectronics, School of Physics, Peking University, Beijing 100871, China;* orcid.org/0000-0003-3140-7842

Zhihua Liang − *Guangdong Basic Research Center of Excellence for Structure and Fundamental Interactions of Matter, Guangdong Provincial Key Laboratory of Quantum Engineering and Quantum Materials, School of Physics, South China Normal University, Guangzhou 510631, China; Guangdong−Hong Kong Joint Laboratory of Quantum Matter, Frontier Research Institute for Physics, South China Normal University, Guangzhou 510631, China*

Fankai Zeng − *Guangdong Basic Research Center of Excellence for Structure and Fundamental Interactions of Matter, Guangdong Provincial Key Laboratory of Quantum Engineering and Quantum Materials, School of Physics, South China Normal University, Guangzhou 510631, China; Guangdong−Hong Kong Joint Laboratory of Quantum Matter, Frontier Research Institute for Physics, South China Normal University, Guangzhou 510631, China*

Xiaowen Zhang − *Guangdong Basic Research Center of Excellence for Structure and Fundamental Interactions of Matter, Guangdong Provincial Key Laboratory of Quantum Engineering and Quantum Materials, School of Physics, South China Normal University, Guangzhou 510631, China; Guangdong−Hong Kong Joint Laboratory of Quantum Matter, Frontier Research Institute for Physics, South China Normal University, Guangzhou 510631, China*

Complete contact information is available at: https://pubs.acs.org/10.1021/prechem.3c00122

Author Contributions

#G.C., J.Q., Z.L., and F.Z. contributed equally to this work

Notes

The authors declare no competing financial interest.

ACKNOWLEDGMENTS

This work was supported by Guangdong Major Project of Basic and Applied Basic Research (2021B030103000), the National Natural Science Foundation of China (12322406, 52102043, 52025023, 51991342, 52021006 and 61905215), the Key R&D Program of Guangdong Province (2020B010189001, 2019B010931001, 2018B010109009 and 2018B030327001), the Pearl River Talent Recruitment Program of Guangdong Province (2019ZT08C321), the Key Project of Science and Technology of Guangzhou (202201010383), the Natural Science Foundation of Guangdong Provinces (2023A1515012743), the Strategic Priority Research Program of Chinese Academy of Sciences (XDB3300000), and the New Cornerstone Science Foundation through the XPLORER PRIZE.

REFERENCES

(1) Novoselov, K. S.; Geim, A. K.; Morozov, S. V.; Jiang, D.-e.; Zhang, Y.; Dubonos, S. V.; Grigorieva, I. V.; Firsov, A. A. Electric field effect in atomically thin carbon films. *Science* **2004**, *306*, 666−669.

(2) Ma, Q.; Ren, G.; Xu, K.; Ou, J. Z. Tunable Optical Properties of 2D Materials and Their Applications. *Adv. Opt. Mater.* **2021**, *9*, 2001313.

(3) Novoselov, K. S.; Jiang, Z.; Zhang, Y.; Morozov, S. V.; Stormer, H. L.; Zeitler, U.; Maan, J. C.; Boebinger, G. S.; Kim, P.; Geim, A. K. Room-temperature quantum Hall effect in graphene. *Science* **2007**, *315*, 1379−1379.

(4) Lagoin, C.; Suffit, S.; Baldwin, K.; Pfeiffer, L.; Dubin, F. Mott insulator of strongly interacting two-dimensional semiconductor excitons. *Nat. Phys.* **2022**, *18*, 149−153.

(5) Bøttcher, C. G. L.; Nichele, F.; Kjaergaard, M.; Suominen, H. J.; Shabani, J.; Palmstrøm, C. J.; Marcus, C. M. Superconducting, insulating and anomalous metallic regimes in a gated two-dimensional semiconductor-superconductor array. *Nat. Phys.* **2018**, *14*, 1138−1144.

(6) Cai, J.; Anderson, E.; Wang, C.; Zhang, X.; Liu, X.; Holtzmann, W.; Zhang, Y.; Fan, F.; Taniguchi, T.; Watanabe, K.; Ran, Y.; Cao, T.; Fu, L.; Xiao, D.; Yao, W.; Xu, X. Signatures of fractional quantum anomalous Hall states in twisted $MoTe_2$. *Nature* **2023**, *622*, 63−68.

(7) Kang, K.; Xie, S.; Huang, L.; Han, Y.; Huang, P. Y.; Mak, K. F.; Kim, C. J.; Muller, D.; Park, J. High-mobility three-atom-thick semiconducting films with wafer-scale homogeneity. *Nature* **2015**, *520*, 656−660.

(8) Radisavljevic, B.; Radenovic, A.; Brivio, J.; Giacometti, V.; Kis, A. Single-layer MoS_2 transistors. *Nat. Nanotechnol.* **2011**, *6*, 147−150.

(9) Chhowalla, M.; Shin, H. S.; Eda, G.; Li, L. J.; Loh, K. P.; Zhang, H. The chemistry of two-dimensional layered transition metal dichalcogenide nanosheets. *Nat. Chem.* **2013**, *5*, 263−275.
(10) Qian, X.; Liu, J.; Fu, L.; Li, J. Quantum spin Hall effect in two-dimensional transition metal dichalcogenides. *Science* **2014**, *346*, 1344−1347.
(11) Novoselov, K. S.; Mishchenko, A.; Carvalho, A.; Castro Neto, A. H. 2D materials and van der Waals heterostructures. *Science* **2016**, *353*, aac9439.
(12) Mak, K. F.; Shan, J. Photonics and optoelectronics of 2D semiconductor transition metal dichalcogenides. *Nat. Photonics* **2016**, *10*, 216−226.
(13) Xu, X.; Qiao, R.; Liang, Z.; Zhang, Z.; Wang, R.; Zeng, F.; Cui, G.; Zhang, X.; Zou, D.; Guo, Y.; et al. Towards intrinsically pure graphene grown on copper. *Nano Res.* **2022**, *15*, 919−924.
(14) Gibb, A. L.; Alem, N.; Chen, J.-H.; Erickson, K. J.; Ciston, J.; Gautam, A.; Linck, M.; Zettl, A. Atomic resolution imaging of grain boundary defects in monolayer chemical vapor deposition-grown hexagonal boron nitride. *J. Am. Chem. Soc.* **2013**, *135*, 6758−6761.
(15) Chandni, U.; Watanabe, K.; Taniguchi, T.; Eisenstein, J. Evidence for defect-mediated tunneling in hexagonal boron nitride-based junctions. *Nano Lett.* **2015**, *15*, 7329−7333.
(16) Najmaei, S.; Liu, Z.; Zhou, W.; Zou, X.; Shi, G.; Lei, S.; Yakobson, B. I.; Idrobo, J.-C.; Ajayan, P. M.; Lou, J. Vapour phase growth and grain boundary structure of molybdenum disulphide atomic layers. *Nat. Mater.* **2013**, *12*, 754−759.
(17) Yu, H.; Yang, Z.; Du, L.; Zhang, J.; Shi, J.; Chen, W.; Chen, P.; Liao, M.; Zhao, J.; Meng, J.; et al. Precisely Aligned Monolayer MoS_2 epitaxially grown on h BN basal plane. *Small* **2017**, *13*, 1603005.
(18) Shen, Y.; Zheng, W.; Zhu, K.; Xiao, Y.; Wen, C.; Liu, Y.; Jing, X.; Lanza, M. Variability and Yield in h BN Based Memristive Circuits: The Role of Each Type of Defect. *Adv. Mater.* **2021**, *33*, 2103656.
(19) Ly, T. H.; Perello, D. J.; Zhao, J.; Deng, Q.; Kim, H.; Han, G. H.; Chae, S. H.; Jeong, H. Y.; Lee, Y. H. Misorientation-angle-dependent electrical transport across molybdenum disulfide grain boundaries. *Nat. Commun.* **2016**, *7*, 10426.
(20) Van Der Zande, A. M.; Huang, P. Y.; Chenet, D. A.; Berkelbach, T. C.; You, Y.; Lee, G.-H.; Heinz, T. F.; Reichman, D. R.; Muller, D. A.; Hone, J. C. Grains and grain boundaries in highly crystalline monolayer molybdenum disulphide. *Nat. Mater.* **2013**, *12*, 554−561.
(21) Wang, J.; Xu, X.; Qiao, R.; Liang, J.; Liu, C.; Zheng, B.; Liu, L.; Gao, P.; Jiao, Q.; Yu, D.; Zhao, Y.; Liu, K. Visualizing grain boundaries in monolayer $MoSe_2$ using mild H_2O vapor etching. *Nano Res.* **2018**, *11*, 4082−4089.
(22) Xu, X.; Zhang, Z.; Dong, J.; Yi, D.; Niu, J.; Wu, M.; Lin, L.; Yin, R.; Li, M.; Zhou, J.; Wang, S.; Sun, J.; Duan, X.; Gao, P.; Jiang, Y.; Wu, X.; Peng, H.; Ruoff, R. S.; Liu, Z.; Yu, D.; Wang, E.; Ding, F.; Liu, K. Ultrafast epitaxial growth of metre-sized single-crystal graphene on industrial Cu foil. *Sci. Bull.* **2017**, *62*, 1074−1080.
(23) Wu, T.; Zhang, X.; Yuan, Q.; Xue, J.; Lu, G.; Liu, Z.; Wang, H.; Wang, H.; Ding, F.; Yu, Q.; Xie, X.; Jiang, M. Fast growth of inch-sized single-crystalline graphene from a controlled single nucleus on Cu-Ni alloys. *Nat. Mater.* **2016**, *15*, 43−47.
(24) Vlassiouk, I. V.; Stehle, Y.; Pudasaini, P. R.; Unocic, R. R.; Rack, P. D.; Baddorf, A. P.; Ivanov, I. N.; Lavrik, N. V.; List, F.; Gupta, N.; et al. Evolutionary selection growth of two-dimensional materials on polycrystalline substrates. *Nat. Mater.* **2018**, *17*, 318−322.
(25) Lin, L.; Li, J.; Ren, H.; Koh, A. L.; Kang, N.; Peng, H.; Xu, H.; Liu, Z. Surface engineering of copper foils for growing centimeter-sized single-crystalline graphene. *ACS Nano* **2016**, *10*, 2922−2929.
(26) Yan, Z.; Lin, J.; Peng, Z.; Sun, Z.; Zhu, Y.; Li, L.; Xiang, C.; Samuel, E. L.; Kittrell, C.; Tour, J. M. Toward the synthesis of wafer-scale single-crystal graphene on copper foils. *ACS Nano* **2012**, *6*, 9110−9117.
(27) Ding, D.; Solís-Fernández, P.; Hibino, H.; Ago, H. Spatially controlled nucleation of single-crystal graphene on Cu assisted by stacked Ni. *ACS Nano* **2016**, *10*, 11196−11204.
(28) Zhou, H.; Yu, W. J.; Liu, L.; Cheng, R.; Chen, Y.; Huang, X.; Liu, Y.; Wang, Y.; Huang, Y.; Duan, X. Chemical vapour deposition growth of large single crystals of monolayer and bilayer graphene. *Nat. Commun.* **2013**, *4*, 2096.
(29) Li, J.; Wang, X.-Y.; Liu, X.-R.; Jin, Z.; Wang, D.; Wan, L.-J. Facile growth of centimeter-sized single-crystal graphene on copper foil at atmospheric pressure. *J. Mater. Chem. C* **2015**, *3*, 3530−3535.
(30) Mohsin, A.; Liu, L.; Liu, P.; Deng, W.; Ivanov, I. N.; Li, G.; Dyck, O. E.; Duscher, G.; Dunlap, J. R.; Xiao, K.; Gu, G. Synthesis of millimeter-size hexagon-shaped graphene single crystals on resolidified copper. *ACS Nano* **2013**, *7*, 8924−8931.
(31) Hao, Y.; Bharathi, M.; Wang, L.; Liu, Y.; Chen, H.; Nie, S.; Wang, X.; Chou, H.; Tan, C.; Fallahazad, B.; et al. The role of surface oxygen in the growth of large single-crystal graphene on copper. *Science* **2013**, *342*, 720−723.
(32) Zhang, J.; Lin, L.; Jia, K.; Sun, L.; Peng, H.; Liu, Z. Controlled Growth of Single-Crystal Graphene Films. *Adv. Mater.* **2020**, *32*, 1903266.
(33) Nguyen, V. L.; Shin, B. G.; Duong, D. L.; Kim, S. T.; Perello, D.; Lim, Y. J.; Yuan, Q. H.; Ding, F.; Jeong, H. Y.; Shin, H. S.; Lee, S. M.; Chae, S. H.; Vu, Q. A.; Lee, S. H.; Lee, Y. H. Seamless stitching of graphene domains on polished copper (111) foil. *Adv. Mater.* **2015**, *27*, 1376−1382.
(34) Wu, M.; Zhang, Z.; Xu, X.; Zhang, Z.; Duan, Y.; Dong, J.; Qiao, R.; You, S.; Wang, L.; Qi, J.; Zou, D.; Shang, N.; Yang, Y.; Li, H.; Zhu, L.; Sun, J.; Yu, H.; Gao, P.; Bai, X.; Jiang, Y.; Wang, Z. J.; Ding, F.; Yu, D.; Wang, E.; Liu, K. Seeded growth of large single-crystal copper foils with high-index facets. *Nature* **2020**, *581*, 406−410.
(35) Li, Y.; Sun, L.; Chang, Z.; Liu, H.; Wang, Y.; Liang, Y.; Chen, B.; Ding, Q.; Zhao, Z.; Wang, R.; et al. Large single crystal cu foils with high index facets by strain engineered anomalous grain growth. *Adv. Mater.* **2020**, *32*, 2002034.
(36) Hou, Y.; Wang, B.; Zhan, L.; Qing, F.; Wang, X.; Niu, X.; Li, X. Surface crystallographic structure insensitive growth of oriented graphene domains on Cu substrates. *Mater. Today* **2020**, *36*, 10−17.
(37) Lee, J. H.; Lee, E. K.; Joo, W. J.; Jang, Y.; Kim, B. S.; Lim, J. Y.; Choi, S. H.; Ahn, S. J.; Ahn, J. R.; Park, M. H.; Yang, C. W.; Choi, B. L.; Hwang, S. W.; Whang, D. Wafer-scale growth of single-crystal monolayer graphene on reusable hydrogen-terminated germanium. *Science* **2014**, *344*, 286−289.
(38) Li, P.; Wei, W.; Zhang, M.; Mei, Y.; Chu, P. K.; Xie, X.; Yuan, Q.; Di, Z. Wafer-scale growth of single-crystal graphene on vicinal Ge(001) substrate. *Nano Today* **2020**, *34*, 100908.
(39) Kang, H.; Tang, P.; Shu, H.; Zhang, Y.; Liang, Y.; Li, J.; Chen, Z.; Sui, Y.; Hu, S.; Wang, S.; Zhao, S.; Zhang, X.; Jiang, C.; Chen, Y.; Xue, Z.; Zhang, M.; Jiang, D.; Yu, G.; Peng, S.; Jin, Z.; Liu, X. Epitaxial growth of wafer scale antioxidant single-crystal graphene on twinned Pt(111). *Carbon* **2021**, *181*, 225−233.
(40) Deng, B.; Xin, Z.; Xue, R.; Zhang, S.; Xu, X.; Gao, J.; Tang, J.; Qi, Y.; Wang, Y.; Zhao, Y.; Sun, L.; Wang, H.; Liu, K.; Rummeli, M. H.; Weng, L. T.; Luo, Z.; Tong, L.; Zhang, X.; Xie, C.; Liu, Z.; Peng, H. Scalable and ultrafast epitaxial growth of single-crystal graphene wafers for electrically tunable liquid-crystal microlens arrays. *Sci. Bull.* **2019**, *64*, 659−668.
(41) Song, X.; Gao, J.; Nie, Y.; Gao, T.; Sun, J.; Ma, D.; Li, Q.; Chen, Y.; Jin, C.; Bachmatiuk, A.; et al. Chemical vapor deposition growth of large-scale hexagonal boron nitride with controllable orientation. *Nano Res.* **2015**, *8*, 3164−3176.
(42) Liu, L.; Wu, J.; Wu, L.; Ye, M.; Liu, X.; Wang, Q.; Hou, S.; Lu, P.; Sun, L.; Zheng, J.; et al. Phase-selective synthesis of 1T′ MoS_2 monolayers and heterophase bilayers. *Nat. Mater.* **2018**, *17*, 1108−1114.
(43) Ruzmetov, D.; Zhang, K.; Stan, G.; Kalanyan, B.; Bhimanapati, G. R.; Eichfeld, S. M.; Burke, R. A.; Shah, P. B.; O'Regan, T. P.; Crowne, F. J.; et al. Vertical 2D/3D semiconductor heterostructures based on epitaxial molybdenum disulfide and gallium nitride. *ACS Nano* **2016**, *10*, 3580−3588.
(44) Zhu, H.; Nayir, N.; Choudhury, T. H.; Bansal, A.; Huet, B.; Zhang, K.; Puretzky, A. A.; Bachu, S.; York, K.; Mc Knight, T. V.; et al. Step engineering for nucleation and domain orientation control in

WSe_2 epitaxy on c-plane sapphire. *Nat. Nanotechnol.* **2023**, *18*, 1295−1302.
(45) Gao, J.; Yip, J.; Zhao, J.; Yakobson, B. I.; Ding, F. Graphene nucleation on transition metal surface: structure transformation and role of the metal step edge. *J. Am. Chem. Soc.* **2011**, *133*, 5009−5015.
(46) Han, G. H.; Gunes, F.; Bae, J. J.; Kim, E. S.; Chae, S. J.; Shin, H. J.; Choi, J. Y.; Pribat, D.; Lee, Y. H. Influence of copper morphology in forming nucleation seeds for graphene growth. *Nano Lett.* **2011**, *11*, 4144−4148.
(47) Chen, H.; Zhu, W.; Zhang, Z. Contrasting behavior of carbon nucleation in the initial stages of graphene epitaxial growth on stepped metal surfaces. *Phys. Rev. Lett.* **2010**, *104*, 186101.
(48) Gao, L.; Ren, W.; Xu, H.; Jin, L.; Wang, Z.; Ma, T.; Ma, L. P.; Zhang, Z.; Fu, Q.; Peng, L. M.; Bao, X.; Cheng, H. M. Repeated growth and bubbling transfer of graphene with millimetre-size single-crystal grains using platinum. *Nat. Commun.* **2012**, *3*, 699.
(49) Geng, D.; Wu, B.; Guo, Y.; Huang, L.; Xue, Y.; Chen, J.; Yu, G.; Jiang, L.; Hu, W.; Liu, Y. Uniform hexagonal graphene flakes and films grown on liquid copper surface. *Proc. Natl. Acad. Sci. U. S. A.* **2012**, *109*, 7992−7996.
(50) Chen, J.; Zhao, X.; Tan, S. J.; Xu, H.; Wu, B.; Liu, B.; Fu, D.; Fu, W.; Geng, D.; Liu, Y.; Liu, W.; Tang, W.; Li, L.; Zhou, W.; Sum, T. C.; Loh, K. P. Chemical Vapor Deposition of Large-Size Monolayer $MoSe_2$ Crystals on Molten Glass. *J. Am. Chem. Soc.* **2017**, *139*, 1073−1076.
(51) Chang, M.-C.; Ho, P.-H.; Tseng, M.-F.; Lin, F.-Y.; Hou, C.-H.; Lin, I. K.; Wang, H.; Huang, P.-P.; Chiang, C.-H.; Yang, Y.-C.; Wang, I. T.; Du, H.-Y.; Wen, C.-Y.; Shyue, J.-J.; Chen, C.-W.; Chen, K.-H.; Chiu, P.-W.; Chen, L.-C. Fast growth of large-grain and continuous MoS_2 films through a self-capping vapor-liquid-solid method. *Nat. Commun.* **2020**, *11*, 3682.
(52) Dong, J.; Zhang, L.; Dai, X.; Ding, F. The epitaxy of 2D materials growth. *Nat. Commun.* **2020**, *11*, 5862.
(53) Zheng, P.; Wei, W.; Liang, Z.; Qin, B.; Tian, J.; Wang, J.; Qiao, R.; Ren, Y.; Chen, J.; Huang, C.; Zhou, X.; Zhang, G.; Tang, Z.; Yu, D.; Ding, F.; Liu, K.; Xu, X. Universal epitaxy of non-centrosymmetric two-dimensional single-crystal metal dichalcogenides. *Nat. Commun.* **2023**, *14*, 592.
(54) Li, T.; Guo, W.; Ma, L.; Li, W.; Yu, Z.; Han, Z.; Gao, S.; Liu, L.; Fan, D.; Wang, Z.; Yang, Y.; Lin, W.; Luo, Z.; Chen, X.; Dai, N.; Tu, X.; Pan, D.; Yao, Y.; Wang, P.; Nie, Y.; Wang, J.; Shi, Y.; Wang, X. Epitaxial growth of wafer-scale molybdenum disulfide semiconductor single crystals on sapphire. *Nat. Nanotechnol.* **2021**, *16*, 1201−1207.
(55) Fu, J. H.; Min, J.; Chang, C. K.; Tseng, C. C.; Wang, Q.; Sugisaki, H.; Li, C.; Chang, Y. M.; Alnami, I.; Syong, W. R.; Lin, C.; Fang, F.; Zhao, L.; Lo, T. H.; Lai, C. S.; Chiu, W. S.; Jian, Z. S.; Chang, W. H.; Lu, Y. J.; Shih, K.; Li, L. J.; Wan, Y.; Shi, Y.; Tung, V. Oriented lateral growth of two-dimensional materials on c-plane sapphire. *Nat. Nanotechnol.* **2023**, *18*, 1289−1294.
(56) Wang, L.; Xu, X.; Zhang, L.; Qiao, R.; Wu, M.; Wang, Z.; Zhang, S.; Liang, J.; Zhang, Z.; Zhang, Z.; Chen, W.; Xie, X.; Zong, J.; Shan, Y.; Guo, Y.; Willinger, M.; Wu, H.; Li, Q.; Wang, W.; Gao, P.; Wu, S.; Zhang, Y.; Jiang, Y.; Yu, D.; Wang, E.; Bai, X.; Wang, Z. J.; Ding, F.; Liu, K. Epitaxial growth of a 100-square-centimetre single-crystal hexagonal boron nitride monolayer on copper. *Nature* **2019**, *570*, 91−95.
(57) Chen, T.-A.; Chuu, C.-P.; Tseng, C.-C.; Wen, C.-K.; Wong, H. S. P.; Pan, S.; Li, R.; Chao, T.-A.; Chueh, W.-C.; Zhang, Y.; Fu, Q.; Yakobson, B. I.; Chang, W.-H.; Li, L.-J. Wafer-scale single-crystal hexagonal boron nitride monolayers on Cu (111). *Nature* **2020**, *579*, 219−223.
(58) Lee, J. S.; Choi, S. H.; Yun, S. J.; Kim, Y. I.; Boandoh, S.; Park, J.-H.; Shin, B. G.; Ko, H.; Lee, S. H.; Kim, Y.-M.; et al. Wafer-scale single-crystal hexagonal boron nitride film via self-collimated grain formation. *Science* **2018**, *362*, 817−821.
(59) Zhang, Q.; Chen, H.; Liu, S.; Yu, Y.; Wang, C.; Han, J.; Shao, G.; Yao, Z. Self-aligned stitching growth of centimeter-scale quasi-single-crystalline hexagonal boron nitride monolayers on liquid copper. *Nanoscale* **2022**, *14*, 3112−3122.
(60) Yang, P.; Zhang, S.; Pan, S.; Tang, B.; Liang, Y.; Zhao, X.; Zhang, Z.; Shi, J.; Huan, Y.; Shi, Y.; Pennycook, S. J.; Ren, Z.; Zhang, G.; Chen, Q.; Zou, X.; Liu, Z.; Zhang, Y. Epitaxial Growth of Centimeter-Scale Single-Crystal MoS_2 Monolayer on Au(111). *ACS Nano* **2020**, *14*, 5036−5045.
(61) Wang, J.; Xu, X.; Cheng, T.; Gu, L.; Qiao, R.; Liang, Z.; Ding, D.; Hong, H.; Zheng, P.; Zhang, Z.; Zhang, Z.; Zhang, S.; Cui, G.; Chang, C.; Huang, C.; Qi, J.; Liang, J.; Liu, C.; Zuo, Y.; Xue, G.; Fang, X.; Tian, J.; Wu, M.; Guo, Y.; Yao, Z.; Jiao, Q.; Liu, L.; Gao, P.; Li, Q.; Yang, R.; Zhang, G.; Tang, Z.; Yu, D.; Wang, E.; Lu, J.; Zhao, Y.; Wu, S.; Ding, F.; Liu, K. Dual-coupling-guided epitaxial growth of wafer-scale single-crystal WS_2 monolayer on vicinal a-plane sapphire. *Nat. Nanotechnol.* **2022**, *17*, 33−38.
(62) Ma, K. Y.; Zhang, L.; Jin, S.; Wang, Y.; Yoon, S. I.; Hwang, H.; Oh, J.; Jeong, D. S.; Wang, M.; Chatterjee, S.; Kim, G.; Jang, A. R.; Yang, J.; Ryu, S.; Jeong, H. Y.; Ruoff, R. S.; Chhowalla, M.; Ding, F.; Shin, H. S. Epitaxial single-crystal hexagonal boron nitride multilayers on Ni (111). *Nature* **2022**, *606*, 88−93.
(63) Chang, C.; Kou, J.-Z.; Xu, X.-Z. Growth of two-dimensional single crystal materials controlled by atomic steps. *Acta Phys. Sin.* **2023**, *72*, 208101.
(64) Knobloch, T.; Illarionov, Y. Y.; Ducry, F.; Schleich, C.; Wachter, S.; Watanabe, K.; Taniguchi, T.; Mueller, T.; Waltl, M.; Lanza, M.; Vexler, M. I.; Luisier, M.; Grasser, T. The performance limits of hexagonal boron nitride as an insulator for scaled CMOS devices based on two-dimensional materials. *Nat. Electron.* **2021**, *4*, 98−108.
(65) Gong, Y.; Xu, Z.-Q.; Li, D.; Zhang, J.; Aharonovich, I.; Zhang, Y. Two-dimensional hexagonal boron nitride for building next-generation energy-efficient devices. *ACS Energy Lett.* **2021**, *6*, 985−996.
(66) Iyikanat, F.; Konecna, A.; Garcia de Abajo, F. J. Nonlinear tunable vibrational response in hexagonal boron nitride. *ACS Nano* **2021**, *15*, 13415−13426.
(67) Wang, N.; Yang, G.; Wang, H.; Yan, C.; Sun, R.; Wong, C.-P. A universal method for large-yield and high-concentration exfoliation of two-dimensional hexagonal boron nitride nanosheets. *Mater. Today* **2019**, *27*, 33−42.
(68) Zhou, H.; Zhu, J.; Liu, Z.; Yan, Z.; Fan, X.; Lin, J.; Wang, G.; Yan, Q.; Yu, T.; Ajayan, P. M.; Tour, J. M. High thermal conductivity of suspended few-layer hexagonal boron nitride sheets. *Nano Res.* **2014**, *7*, 1232−1240.
(69) Zhang, J.; Tan, B.; Zhang, X.; Gao, F.; Hu, Y.; Wang, L.; Duan, X.; Yang, Z.; Hu, P. Atomically Thin Hexagonal Boron Nitride and Its Heterostructures. *Adv. Mater.* **2021**, *33*, 2000769.
(70) Tran, T. T.; Bray, K.; Ford, M. J.; Toth, M.; Aharonovich, I. Quantum emission from hexagonal boron nitride monolayers. *Nat. Nanotechnol.* **2016**, *11*, 37−41.
(71) Li, X.; Long, Y.; Ma, L.; Li, J.; Yin, J.; Guo, W. Coating performance of hexagonal boron nitride and graphene layers. *2D Mater.* **2021**, *8*, 034002.
(72) Wang, L.; Qi, J.; Zhang, S.; Ding, M.; Wei, W.; Wang, J.; Zhang, Z.; Qiao, R.; Zhang, Z.; Li, Z.; Liu, K.; Fu, Y.; Hong, H.; Liu, C.; Wu, M.; Wang, W.; He, J.; Cui, Y.; Li, Q.; Bai, X.; Liu, K. Abnormal anti-oxidation behavior of hexagonal boron nitride grown on copper. *Nano Res.* **2022**, *15*, 7577−7583.
(73) Shi, Y.; Hamsen, C.; Jia, X.; Kim, K. K.; Reina, A.; Hofmann, M.; Hsu, A. L.; Zhang, K.; Li, H.; Juang, Z. Y.; Dresselhaus, M. S.; Li, L. J.; Kong, J. Synthesis of few-layer hexagonal boron nitride thin film by chemical vapor deposition. *Nano Lett.* **2010**, *10*, 4134−4139.
(74) Ismach, A.; Chou, H.; Ferrer, D. A.; Wu, Y.; McDonnell, S.; Floresca, H. C.; Covacevich, A.; Pope, C.; Piner, R.; Kim, M. J.; et al. Toward the controlled synthesis of hexagonal boron nitride films. *ACS Nano* **2012**, *6*, 6378−6385.
(75) Xiaozhi, X.; Xiaowen, Z.; Ran, W.; Fankai, Z.; Tao, Z. The Research Progress on the Growth of Wafer-scale Two-Dimensional Single-crystal Materials. *J. South China Norm. Univ.* **2021**, *53*, 1−8.
(76) Tay, R. Y.; Griep, M. H.; Mallick, G.; Tsang, S. H.; Singh, R. S.; Tumlin, T.; Teo, E. H.; Karna, S. P. Growth of large single-crystalline two-dimensional boron nitride hexagons on electropolished copper. *Nano Lett.* **2014**, *14*, 839−846.
(77) Tian, H.; He, Y.; Das, P.; Cui, Z.; Shi, W.; Khanaki, A.; Lake, R. K.; Liu, J. Growth Dynamics of Millimeter Sized Single Crystal

Hexagonal Boron Nitride Monolayers on Secondary Recrystallized Ni (100) Substrates. *Adv. Mater. Interfaces* **2019**, *6*, 1091198.
(78) Lu, G.; Wu, T.; Yuan, Q.; Wang, H.; Wang, H.; Ding, F.; Xie, X.; Jiang, M. Synthesis of large single-crystal hexagonal boron nitride grains on Cu-Ni alloy. *Nat. Commun.* **2015**, *6*, 6160.
(79) Caneva, S.; Weatherup, R. S.; Bayer, B. C.; Brennan, B.; Spencer, S. J.; Mingard, K.; Cabrero-Vilatela, A.; Baehtz, C.; Pollard, A. J.; Hofmann, S. Nucleation control for large, single crystalline domains of monolayer hexagonal boron nitride via Si-doped Fe catalysts. *Nano Lett.* **2015**, *15*, 1867−1875.
(80) Li, J.; Hu, Z.; Yi, Y.; Yu, M.; Li, X.; Zhou, J.; Yin, J.; Wu, S.; Guo, W. Hexagonal Boron Nitride Growth on Cu-Si Alloy: Morphologies and Large Domains. *Small* **2019**, *15*, 1805188.
(81) Chang, R.-J.; Wang, X.; Wang, S.; Sheng, Y.; Porter, B.; Bhaskaran, H.; Warner, J. H. Growth of Large Single-Crystalline Monolayer Hexagonal Boron Nitride by Oxide-Assisted Chemical Vapor Deposition. *Chem. Mater.* **2017**, *29*, 6252−6260.
(82) Li, M.; Zhou, S.; Wang, R.; Yu, Y.; Wong, H.; Luo, Z.; Li, H.; Gan, L.; Zhai, T. In situ formed nanoparticle-assisted growth of large-size single crystalline h-BN on copper. *Nanoscale* **2018**, *10*, 17865−17872.
(83) Ji, Y.; Calderon, B.; Han, Y.; Cueva, P.; Jungwirth, N. R.; Alsalman, H. A.; Hwang, J.; Fuchs, G. D.; Muller, D. A.; Spencer, M. G. Chemical Vapor Deposition Growth of Large Single-Crystal Mono-, Bi-, Tri-Layer Hexagonal Boron Nitride and Their Interlayer Stacking. *ACS Nano* **2017**, *11*, 12057−12066.
(84) Zhu, T.; Liang, Y.; Zhang, C.; Wang, Z.; Dong, M.; Wang, C.; Yang, M.; Goto, T.; Tu, R.; Zhang, S. A high-throughput synthesis of large-sized single-crystal hexagonal boron nitride on a Cu-Ni gradient enclosure. *RSC Adv.* **2020**, *10*, 16088−16093.
(85) Wu, Q.; Park, J.-H.; Park, S.; Jung, S. J.; Suh, H.; Park, N.; Wongwiriyapan, W.; Lee, S.; Lee, Y. H.; Song, Y. J. Single crystalline film of hexagonal boron nitride atomic monolayer by controlling nucleation seeds and domains. *Sci. Rep.* **2015**, *5*, 16159.
(86) Caneva, S.; Weatherup, R. S.; Bayer, B. C.; Blume, R.; Cabrero-Vilatela, A.; Braeuninger-Weimer, P.; Martin, M. B.; Wang, R.; Baehtz, C.; Schloegl, R.; Meyer, J. C.; Hofmann, S. Controlling Catalyst Bulk Reservoir Effects for Monolayer Hexagonal Boron Nitride CVD. *Nano Lett.* **2016**, *16*, 1250−1261.
(87) Wang, L.; Wu, B.; Liu, H.; Huang, L.; Li, Y.; Guo, W.; Chen, X.; Peng, P.; Fu, L.; Yang, Y.; Hu, P.; Liu, Y. Water-assisted growth of large-sized single crystal hexagonal boron nitride grains. *Mater. Chem. Front.* **2017**, *1*, 1836−1840.
(88) Liu, C.; Xu, X.; Qiu, L.; Wu, M.; Qiao, R.; Wang, L.; Wang, J.; Niu, J.; Liang, J.; Zhou, X.; Zhang, Z.; Peng, M.; Gao, P.; Wang, W.; Bai, X.; Ma, D.; Jiang, Y.; Wu, X.; Yu, D.; Wang, E.; Xiong, J.; Ding, F.; Liu, K. Kinetic modulation of graphene growth by fluorine through spatially confined decomposition of metal fluorides. *Nat. Chem.* **2019**, *11*, 730−736.
(89) Wang, S.; Dearle, A. E.; Maruyama, M.; Ogawa, Y.; Okada, S.; Hibino, H.; Taniyasu, Y. Catalyst-Selective Growth of Single-Orientation Hexagonal Boron Nitride toward High-Performance Atomically Thin Electric Barriers. *Adv. Mater.* **2019**, *31*, 1900880.
(90) Li, J.; Li, Y.; Yin, J.; Ren, X.; Liu, X.; Jin, C.; Guo, W. Growth of Polar Hexagonal Boron Nitride Monolayer on Nonpolar Copper with Unique Orientation. *Small* **2016**, *12*, 3645−3650.
(91) Tan, L.; Han, J.; Mendes, R. G.; Rümmeli, M. H.; Liu, J.; Wu, Q.; Leng, X.; Zhang, T.; Zeng, M.; Fu, L. Self aligned single crystalline hexagonal boron nitride arrays: toward higher integrated electronic devices. *Adv. Electron. Mater.* **2015**, *1*, 1500223.
(92) Li, Y.; Rao, Y.; Mak, K. F.; You, Y.; Wang, S.; Dean, C. R.; Heinz, T. F. Probing Symmetry Properties of Few-Layer MoS_2 and h-BN by Optical Second-Harmonic Generation. *Nano Lett.* **2013**, *13*, 3329−3333.
(93) Kim, C. J.; Brown, L.; Graham, M. W.; Hovden, R.; Havener, R. W.; McEuen, P. L.; Muller, D. A.; Park, J. Stacking order dependent second harmonic generation and topological defects in h-BN bilayers. *Nano Lett.* **2013**, *13*, 5660−5665.
(94) Rousseau, A.; Valvin, P.; Desrat, W.; Xue, L.; Li, J.; Edgar, J. H.; Cassabois, G.; Gil, B. Bernal Boron Nitride Crystals Identified by Deep-Ultraviolet Cryomicroscopy. *ACS Nano* **2022**, *16*, 2756−2761.
(95) Yasuda, K.; Wang, X.; Watanabe, K.; Taniguchi, T.; Jarillo-Herrero, P. Stacking-engineered ferroelectricity in bilayer boron nitride. *Science* **2021**, *372*, 1458−1462.
(96) Stern, M.; Waschitz, Y.; Cao, W.; Nevo, I.; Watanabe, K.; Taniguchi, T.; Sela, E.; Urbakh, M.; Hod, O.; Shalom, M. Interfacial ferroelectricity by van-der-Waals sliding. *Science* **2021**, *372*, 1462−1466.
(97) Hattori, Y.; Taniguchi, T.; Watanabe, K.; Nagashio, K. Layer-by-layer dielectric breakdown of hexagonal boron nitride. *ACS Nano* **2015**, *9*, 916−921.
(98) Das, S.; Sebastian, A.; Pop, E.; McClellan, C. J.; Franklin, A. D.; Grasser, T.; Knobloch, T.; Illarionov, Y.; Penumatcha, A. V.; Appenzeller, J.; et al. Transistors based on two-dimensional materials for future integrated circuits. *Nat. Electron.* **2021**, *4*, 786−799.
(99) Giles, A. J.; Dai, S.; Vurgaftman, I.; Hoffman, T.; Liu, S.; Lindsay, L.; Ellis, C. T.; Assefa, N.; Chatzakis, I.; Reinecke, T. L.; et al. Ultralow-loss polaritons in isotopically pure boron nitride. *Nat. Mater.* **2018**, *17*, 134−139.
(100) Li, P.; Dolado, I.; Alfaro-Mozaz, F. J.; Casanova, F.; Hueso, L. E.; Liu, S.; Edgar, J. H.; Nikitin, A. Y.; Vélez, S.; Hillenbrand, R. Infrared hyperbolic metasurface based on nanostructured van der Waals materials. *Science* **2018**, *359*, 892−896.
(101) Wang, H.; Zhang, X.; Liu, H.; Yin, Z.; Meng, J.; Xia, J.; Meng, X. M.; Wu, J.; You, J. Synthesis of Large Sized Single Crystal Hexagonal Boron Nitride Domains on Nickel Foils by Ion Beam Sputtering Deposition. *Adv. Mater.* **2015**, *27*, 8109−8115.
(102) Tonkikh, A.; Voloshina, E.; Werner, P.; Blumtritt, H.; Senkovskiy, B.; Güntherodt, G.; Parkin, S.; Dedkov, Y. S. Structural and electronic properties of epitaxial multilayer h-BN on Ni (111) for spintronics applications. *Sci. Rep.* **2016**, *6*, 23547.
(103) Vuong, T.; Cassabois, G.; Valvin, P.; Rousseau, E.; Summerfield, A.; Mellor, C.; Cho, Y.; Cheng, T.; Albar, J.; Eaves, L.; et al. Deep ultraviolet emission in hexagonal boron nitride grown by high-temperature molecular beam epitaxy. *2D Mater.* **2017**, *4*, 021023.
(104) Xu, Z.; Tian, H.; Khanaki, A.; Zheng, R.; Suja, M.; Liu, J. Large-area growth of multi-layer hexagonal boron nitride on polished cobalt foils by plasma-assisted molecular beam epitaxy. *Sci. Rep.* **2017**, *7*, 43100.
(105) Page, R.; Casamento, J.; Cho, Y.; Rouvimov, S.; Xing, H. G.; Jena, D. Rotationally aligned hexagonal boron nitride on sapphire by high-temperature molecular beam epitaxy. *Phys. Rev. Mater.* **2019**, *3*, 064001.
(106) Jeong, H.; Kim, D. Y.; Kim, J.; Moon, S.; Han, N.; Lee, S. H.; Okello, O. F. N.; Song, K.; Choi, S.-Y.; Kim, J. K. Wafer-scale and selective-area growth of high-quality hexagonal boron nitride on Ni (111) by metal-organic chemical vapor deposition. *Sci. Rep.* **2019**, *9*, 5736.
(107) Gao, Y.; Ren, W.; Ma, T.; Liu, Z.; Zhang, Y.; Liu, W. B.; Ma, L. P.; Ma, X.; Cheng, H. M. Repeated and controlled growth of monolayer, bilayer and few-layer hexagonal boron nitride on Pt foils. *ACS Nano* **2013**, *7*, 5199−5206.
(108) Zhang, C.; Fu, L.; Zhao, S.; Zhou, Y.; Peng, H.; Liu, Z. Controllable co-segregation synthesis of wafer-scale hexagonal boron nitride thin films. *Adv. Mater.* **2014**, *26*, 1776−1781.
(109) Hui, F.; Villena, M. A.; Fang, W.; Lu, A.-Y.; Kong, J.; Shi, Y.; Jing, X.; Zhu, K.; Lanza, M. Synthesis of large-area multilayer hexagonal boron nitride sheets on iron substrates and its use in resistive switching devices. *2D Mater.* **2018**, *5*, 031011.
(110) Kim, S. M.; Hsu, A.; Park, M. H.; Chae, S. H.; Yun, S. J.; Lee, J. S.; Cho, D.-H.; Fang, W.; Lee, C.; Palacios, T.; Dresselhaus, M.; Kim, K. K.; Lee, Y. H.; Kong, J. Synthesis of large-area multilayer hexagonal boron nitride for high material performance. *Nat. Commun.* **2015**, *6*, 8662.
(111) Uchida, Y.; Nakandakari, S.; Kawahara, K.; Yamasaki, S.; Mitsuhara, M.; Ago, H. Controlled Growth of Large-Area Uniform

Multilayer Hexagonal Boron Nitride as an Effective 2D Substrate. *ACS Nano* **2018**, *12*, 6236−6244.
(112) Fukamachi, S.; Solís-Fernández, P.; Kawahara, K.; Tanaka, D.; Otake, T.; Lin, Y.-C.; Suenaga, K.; Ago, H. Large-area synthesis and transfer of multilayer hexagonal boron nitride for enhanced graphene device arrays. *Nat. Electron.* **2023**, *6*, 126−136.
(113) Yang, P.; Wang, D.; Zhao, X.; Quan, W.; Jiang, Q.; Li, X.; Tang, B.; Hu, J.; Zhu, L.; Pan, S.; et al. Epitaxial growth of inch-scale single-crystal transition metal dichalcogenides through the patching of unidirectionally orientated ribbons. *Nat. Commun.* **2022**, *13*, 3238.
(114) Chen, Z.; Qi, Y.; Chen, X.; Zhang, Y.; Liu, Z. Direct CVD growth of graphene on traditional glass: methods and mechanisms. *Adv. Mater.* **2019**, *31*, 1803639.
(115) Gao, Y.; Hong, Y. L.; Yin, L. C.; Wu, Z.; Yang, Z.; Chen, M. L.; Liu, Z.; Ma, T.; Sun, D. M.; Ni, Z.; et al. Ultrafast growth of high quality monolayer WSe_2 on Au. *Adv. Mater.* **2017**, *29*, 1700990.
(116) Fan, Y.; Li, L.; Yu, G.; Geng, D.; Zhang, X.; Hu, W. Recent Advances in Growth of Large Sized 2D Single Crystals on Cu Substrates. *Adv. Mater.* **2021**, *33*, 2003956.
(117) Zhang, Z.; Ding, M.; Cheng, T.; Qiao, R.; Zhao, M.; Luo, M.; Wang, E.; Sun, Y.; Zhang, S.; Li, X.; Zhang, Z.; Mao, H.; Liu, F.; Fu, Y.; Liu, K.; Zou, D.; Liu, C.; Wu, M.; Fan, C.; Zhu, Q.; Wang, X.; Gao, P.; Li, Q.; Liu, K.; Zhang, Y.; Bai, X.; Yu, D.; Ding, F.; Wang, E.; Liu, K. Continuous epitaxy of single-crystal graphite films by isothermal carbon diffusion through nickel. *Nat. Nanotechnol.* **2022**, *17*, 1258−1264.
(118) Qi, J.; Ma, C.; Guo, Q.; Ma, C.; Zhang, Z.; Liu, F.; Shi, X.; Wang, L.; Xue, M.; Wu, M.; Gao, P.; Hong, H.; Wang, X.; Wang, E.; Liu, C.; Liu, K. Stacking-Controlled Growth of rBN Crystalline Films with High Nonlinear Optical Conversion Efficiency up to 1%. *Adv. Mater.* **2023**, 2303122.
(119) Chia, X.; Pumera, M. Characteristics and performance of two-dimensional materials for electrocatalysis. *Nat. Catal.* **2018**, *1*, 909−921.
(120) Tan, C.; Cao, X.; Wu, X. J.; He, Q.; Yang, J.; Zhang, X.; Chen, J.; Zhao, W.; Han, S.; Nam, G. H.; Sindoro, M.; Zhang, H. Recent Advances in Ultrathin Two-Dimensional Nanomaterials. *Chem. Rev.* **2017**, *117*, 6225−6331.
(121) Daus, A.; Vaziri, S.; Chen, V.; Köroğlu, Ç.; Grady, R. W.; Bailey, C. S.; Lee, H. R.; Schauble, K.; Brenner, K.; Pop, E. High-performance flexible nanoscale transistors based on transition metal dichalcogenides. *Nat. Electron.* **2021**, *4*, 495−501.
(122) Zhang, Y.; Yao, Y.; Sendeku, M. G.; Yin, L.; Zhan, X.; Wang, F.; Wang, Z.; He, J. Recent Progress in CVD Growth of 2D Transition Metal Dichalcogenides and Related Heterostructures. *Adv. Mater.* **2019**, *31*, 1901694.
(123) Wang, Z.; Xie, Y.; Wang, H.; Wu, R.; Nan, T.; Zhan, Y.; Sun, J.; Jiang, T.; Zhao, Y.; Lei, Y.; Yang, M.; Wang, W.; Zhu, Q.; Ma, X.; Hao, Y. NaCl-assisted one-step growth of MoS_2-WS_2 in-plane heterostructures. *Nanotechnol.* **2017**, *28*, 325602.
(124) Li, S.; Wang, S.; Tang, D.-M.; Zhao, W.; Xu, H.; Chu, L.; Bando, Y.; Golberg, D.; Eda, G. Halide-assisted atmospheric pressure growth of large WSe_2 and WS_2 monolayer crystals. *Appl. Mater. Today* **2015**, *1*, 60−66.
(125) Zhou, J.; Lin, J.; Huang, X.; Zhou, Y.; Chen, Y.; Xia, J.; Wang, H.; Xie, Y.; Yu, H.; Lei, J.; Wu, D.; Liu, F.; Fu, Q.; Zeng, Q.; Hsu, C. H.; Yang, C.; Lu, L.; Yu, T.; Shen, Z.; Lin, H.; Yakobson, B. I.; Liu, Q.; Suenaga, K.; Liu, G.; Liu, Z. A library of atomically thin metal chalcogenides. *Nature* **2018**, *556*, 355−359.
(126) Zhou, S.; Liu, L.; Cui, S.; Ping, X.; Hu, D.; Jiao, L. Fast growth of large single-crystalline WS_2 monolayers via chemical vapor deposition. *Nano Res.* **2021**, *14*, 1659−1662.
(127) Tong, X.; Liu, K.; Zeng, M.; Fu, L. Vapor phase growth of high quality wafer scale two dimensional materials. *InfoMat* **2019**, *1*, 460−478.
(128) Wang, H.; Wang, G.; Bao, P.; Yang, S.; Zhu, W.; Xie, X.; Zhang, W. J. Controllable synthesis of submillimeter single-crystal monolayer graphene domains on copper foils by suppressing nucleation. *J. Am. Chem. Soc.* **2012**, *134*, 3627−3630.
(129) Xu, X.; Zhang, Z.; Qiu, L.; Zhuang, J.; Zhang, L.; Wang, H.; Liao, C.; Song, H.; Qiao, R.; Gao, P.; Hu, Z.; Liao, L.; Liao, Z.; Yu, D.; Wang, E.; Ding, F.; Peng, H.; Liu, K. Ultrafast growth of single-crystal graphene assisted by a continuous oxygen supply. *Nat. Nanotechnol.* **2016**, *11*, 930−935.
(130) Zhang, Z.; Xu, X.; Qiu, L.; Wang, S.; Wu, T.; Ding, F.; Peng, H.; Liu, K. The Way towards Ultrafast Growth of Single-Crystal Graphene on Copper. *Adv. Sci.* **2017**, *4*, 1700087.
(131) Tang, S.; Wang, H.; Wang, H. S.; Sun, Q.; Zhang, X.; Cong, C.; Xie, H.; Liu, X.; Zhou, X.; Huang, F.; Chen, X.; Yu, T.; Ding, F.; Xie, X.; Jiang, M. Silane-catalysed fast growth of large single-crystalline graphene on hexagonal boron nitride. *Nat. Commun.* **2015**, *6*, 6499.
(132) Zhang, Z.; Chen, P.; Yang, X.; Liu, Y.; Ma, H.; Li, J.; Zhao, B.; Luo, J.; Duan, X.; Duan, X. Ultrafast growth of large single crystals of monolayer WS_2 and WSe_2. *Natl. Sci. Rev.* **2020**, *7*, 737−744.
(133) Dumcenco, D.; Ovchinnikov, D.; Marinov, K.; Lazic, P.; Gibertini, M.; Marzari, N.; Sanchez, O. L.; Kung, Y.-C.; Krasnozhon, D.; Chen, M.-W.; et al. Large-area epitaxial monolayer MoS_2. *ACS Nano* **2015**, *9*, 4611−4620.
(134) Nakamura, S.; Krames, M. R. History of gallium-nitride-based light-emitting diodes for illumination. *Proc. IEEE* **2013**, *101*, 2211−2220.
(135) Li, J.; Wang, S.; Jiang, Q.; Qian, H.; Hu, S.; Kang, H.; Chen, C.; Zhan, X.; Yu, A.; Zhao, S.; Zhang, Y.; Chen, Z.; Sui, Y.; Qiao, S.; Yu, G.; Peng, S.; Jin, Z.; Liu, X. Single-Crystal MoS_2 Monolayer Wafer Grown on Au (111) Film Substrates. *Small* **2021**, *17*, 2100743.
(136) Tumino, F.; Grazianetti, C.; Martella, C.; Ruggeri, M.; Russo, V.; Li Bassi, A.; Molle, A.; Casari, C. S. Hydrophilic Character of Single-Layer MoS_2 Grown on Ag(111). *J. Phys. Chem. C Nanomater Interfaces* **2021**, *125*, 9479−9485.
(137) Uchida, Y.; Iwaizako, T.; Mizuno, S.; Tsuji, M.; Ago, H. Epitaxial chemical vapour deposition growth of monolayer hexagonal boron nitride on a Cu (111)/sapphire substrate. *Phys. Chem. Chem. Phys.* **2017**, *19*, 8230−8235.
(138) Ma, Z.; Wang, S.; Deng, Q.; Hou, Z.; Zhou, X.; Li, X.; Cui, F.; Si, H.; Zhai, T.; Xu, H. Epitaxial growth of rectangle shape MoS_2 with highly aligned orientation on twofold symmetry a plane sapphire. *Small* **2020**, *16*, 2000596.
(139) Chubarov, M.; Choudhury, T. H.; Hickey, D. R.; Bachu, S.; Zhang, T.; Sebastian, A.; Bansal, A.; Zhu, H.; Trainor, N.; Das, S.; et al. Wafer-scale epitaxial growth of unidirectional WS_2 monolayers on sapphire. *ACS Nano* **2021**, *15*, 2532−2541.
(140) Chen, L.; Liu, B.; Ge, M.; Ma, Y.; Abbas, A. N.; Zhou, C. Step-edge-guided nucleation and growth of aligned WSe_2 on sapphire via a layer-over-layer growth mode. *ACS Nano* **2015**, *9*, 8368−8375.
(141) Choi, S. H.; Kim, H. J.; Song, B.; Kim, Y. I.; Han, G.; Nguyen, H. T. T.; Ko, H.; Boandoh, S.; Choi, J. H.; Oh, C. S.; et al. Epitaxial single crystal growth of transition metal dichalcogenide monolayers via the atomic sawtooth Au surface. *Adv. Mater.* **2021**, *33*, 2006601.
(142) Li, J.; Wang, S.; Jiang, Q.; Qian, H.; Hu, S.; Kang, H.; Chen, C.; Zhan, X.; Yu, A.; Zhao, S.; et al. Single crystal MoS_2 monolayer wafer grown on Au (111) film substrates. *Small* **2021**, *17*, 2100743.
(143) Aljarb, A.; Fu, J.-H.; Hsu, C.-C.; Chuu, C.-P.; Wan, Y.; Hakami, M.; Naphade, D. R.; Yengel, E.; Lee, C.-J.; Brems, S.; et al. Ledge-directed epitaxy of continuously self-aligned single-crystalline nanoribbons of transition metal dichalcogenides. *Nat. Mater.* **2020**, *19*, 1300−1306.
(144) Li, N.; Wang, Q.; Shen, C.; Wei, Z.; Yu, H.; Zhao, J.; Lu, X.; Wang, G.; He, C.; Xie, L.; et al. Large-scale flexible and transparent electronics based on monolayer molybdenum disulfide field-effect transistors. *Nat. Electron.* **2020**, *3*, 711−717.
(145) Wang, Q.; Li, N.; Tang, J.; Zhu, J.; Zhang, Q.; Jia, Q.; Lu, Y.; Wei, Z.; Yu, H.; Zhao, Y.; et al. Wafer-scale highly oriented monolayer MoS_2 with large domain sizes. *Nano Lett.* **2020**, *20*, 7193−7199.
(146) Aljarb, A.; Cao, Z.; Tang, H.-L.; Huang, J.-K.; Li, M.; Hu, W.; Cavallo, L.; Li, L.-J. Substrate lattice-guided seed formation controls the orientation of 2D transition-metal dichalcogenides. *ACS Nano* **2017**, *11*, 9215−9222.

https://doi.org/10.1021/prechem.3c00122
Precis. Chem. 2024, 2, 330−354

(147) Yu, H.; Liao, M.; Zhao, W.; Liu, G.; Zhou, X.; Wei, Z.; Xu, X.; Liu, K.; Hu, Z.; Deng, K.; et al. Wafer-scale growth and transfer of highly-oriented monolayer MoS_2 continuous films. *ACS Nano* **2017**, *11*, 12001−12007.
(148) Grønborg, S. S.; Ulstrup, S.; Bianchi, M.; Dendzik, M.; Sanders, C. E.; Lauritsen, J. V.; Hofmann, P.; Miwa, J. A. Synthesis of epitaxial single-layer MoS_2 on Au (111). *Langmuir* **2015**, *31*, 9700−9706.
(149) Pan, S.; Yang, P.; Zhu, L.; Hong, M.; Xie, C.; Zhou, F.; Shi, Y.; Huan, Y.; Cui, F.; Zhang, Y. Effect of substrate symmetry on the orientations of MoS_2 monolayers. *Nanotechnol.* **2021**, *32*, 095601.
(150) Tay, R. Y.; Park, H. J.; Ryu, G. H.; Tan, D.; Tsang, S. H.; Li, H.; Liu, W.; Teo, E. H. T.; Lee, Z.; Lifshitz, Y.; Ruoff, R. S. Synthesis of aligned symmetrical multifaceted monolayer hexagonal boron nitride single crystals on resolidified copper. *Nanoscale* **2016**, *8*, 2434−2444.
(151) Meng, J.; Zhang, X.; Wang, Y.; Yin, Z.; Liu, H.; Xia, J.; Wang, H.; You, J.; Jin, P.; Wang, D.; Meng, X.-M. Aligned Growth of Millimeter Size Hexagonal Boron Nitride Single Crystal Domains on Epitaxial Nickel Thin Film. *Small* **2017**, *13*, 1604179.
(152) Taslim, A. B.; Nakajima, H.; Lin, Y.-C.; Uchida, Y.; Kawahara, K.; Okazaki, T.; Suenaga, K.; Hibino, H.; Ago, H. Synthesis of sub-millimeter single-crystal grains of aligned hexagonal boron nitride on an epitaxial Ni film. *Nanoscale* **2019**, *11*, 14668−14675.
(153) Yin, J.; Liu, X.; Lu, W.; Li, J.; Cao, Y.; Li, Y.; Xu, Y.; Li, X.; Zhou, J.; Jin, C.; Guo, W. Aligned growth of hexagonal boron nitride monolayer on germanium. *Small* **2015**, *11*, 5375−5380.
(154) Kim, S.; Konar, A.; Hwang, W. S.; Lee, J. H.; Lee, J.; Yang, J.; Jung, C.; Kim, H.; Yoo, J. B.; Choi, J. Y.; Jin, Y. W.; Lee, S. Y.; Jena, D.; Choi, W.; Kim, K. High-mobility and low-power thin-film transistors based on multilayer MoS_2 crystals. *Nat. Commun.* **2012**, *3*, 1011.
(155) Li, Y.; Xu, H.; Liu, W.; Yang, G.; Shi, J.; Liu, Z.; Liu, X.; Wang, Z.; Tang, Q.; Liu, Y. Enhancement of Exciton Emission from Multilayer MoS_2 at High Temperatures: Intervalley Transfer versus Interlayer Decoupling. *Small* **2017**, *13*, 1700157.
(156) Wang, Q.; Tang, J.; Li, X.; Tian, J.; Liang, J.; Li, N.; Ji, D.; Xian, L.; Guo, Y.; Li, L.; Zhang, Q.; Chu, Y.; Wei, Z.; Zhao, Y.; Du, L.; Yu, H.; Bai, X.; Gu, L.; Liu, K.; Yang, W.; Yang, R.; Shi, D.; Zhang, G. Layer-by-layer epitaxy of multi-layer MoS_2 wafers. *Natl. Sci. Rev.* **2022**, *9*, nwac077.
(157) Liu, L.; Li, T.; Ma, L.; Li, W.; Gao, S.; Sun, W.; Dong, R.; Zou, X.; Fan, D.; Shao, L.; Gu, C.; Dai, N.; Yu, Z.; Chen, X.; Tu, X.; Nie, Y.; Wang, P.; Wang, J.; Shi, Y.; Wang, X. Uniform nucleation and epitaxy of bilayer molybdenum disulfide on sapphire. *Nature* **2022**, *605*, 69−75.
(158) Li, X.; Shi, X.; Marian, D.; Soriano, D.; Cusati, T.; Iannaccone, G.; Fiori, G.; Guo, Q.; Zhao, W.; Wu, Y. Rhombohedral-stacked bilayer transition metal dichalcogenides for high-performance atomically thin CMOS devices. *Sci. Adv.* **2023**, *9*, eade5706.
(159) Zhang, X.; Nan, H.; Xiao, S.; Wan, X.; Gu, X.; Du, A.; Ni, Z.; Ostrikov, K. K. Transition metal dichalcogenides bilayer single crystals by reverse-flow chemical vapor epitaxy. *Nat. Commun.* **2019**, *10*, 598.
(160) Shi, J.; Yu, P.; Liu, F.; He, P.; Wang, R.; Qin, L.; Zhou, J.; Li, X.; Zhou, J.; Sui, X.; et al. 3R MoS_2 with broken inversion symmetry: a promising ultrathin nonlinear optical device. *Adv. Mater.* **2017**, *29*, 1701486.
(161) Xu, X.; Trovatello, C.; Mooshammer, F.; Shao, Y.; Zhang, S.; Yao, K.; Basov, D. N.; Cerullo, G.; Schuck, P. J. Towards compact phase-matched and waveguided nonlinear optics in atomically layered semiconductors. *Nat. Photonics* **2022**, *16*, 698−706.
(162) Deb, S.; Cao, W.; Raab, N.; Watanabe, K.; Taniguchi, T.; Goldstein, M.; Kronik, L.; Urbakh, M.; Hod, O.; Ben Shalom, M. Cumulative polarization in conductive interfacial ferroelectrics. *Nature* **2022**, *612*, 465−469.
(163) Weston, A.; Castanon, E. G.; Enaldiev, V.; Ferreira, F.; Bhattacharjee, S.; Xu, S.; Corte-Leon, H.; Wu, Z.; Clark, N.; Summerfield, A.; Hashimoto, T.; Gao, Y.; Wang, W.; Hamer, M.; Read, H.; Fumagalli, L.; Kretinin, A. V.; Haigh, S. J.; Kazakova, O.; Geim, A. K.; Fal'ko, V. I.; Gorbachev, R. Interfacial ferroelectricity in marginally twisted 2D semiconductors. *Nat. Nanotechnol.* **2022**, *17*, 390−395.
(164) Liu, K.; Zhang, L.; Cao, T.; Jin, C.; Qiu, D.; Zhou, Q.; Zettl, A.; Yang, P.; Louie, S. G.; Wang, F. Evolution of interlayer coupling in twisted molybdenum disulfide bilayers. *Nat. Commun.* **2014**, *5*, 4966.
(165) Liao, M.; Wei, Z.; Du, L.; Wang, Q.; Tang, J.; Yu, H.; Wu, F.; Zhao, J.; Xu, X.; Han, B.; Liu, K.; Gao, P.; Polcar, T.; Sun, Z.; Shi, D.; Yang, R.; Zhang, G. Precise control of the interlayer twist angle in large scale MoS_2 homostructures. *Nat. Commun.* **2020**, *11*, 2153.
(166) Liu, C.; Li, Z.; Qiao, R.; Wang, Q.; Zhang, Z.; Liu, F.; Zhou, Z.; Shang, N.; Fang, H.; Wang, M.; Liu, Z.; Feng, Z.; Cheng, Y.; Wu, H.; Gong, D.; Liu, S.; Zhang, Z.; Zou, D.; Fu, Y.; He, J.; Hong, H.; Wu, M.; Gao, P.; Tan, P. H.; Wang, X.; Yu, D.; Wang, E.; Wang, Z. J.; Liu, K. Designed growth of large bilayer graphene with arbitrary twist angles. *Nat. Mater.* **2022**, *21*, 1263−1268.
(167) Liu, F.; Wu, W.; Bai, Y.; Chae, S. H.; Li, Q.; Wang, J.; Hone, J.; Zhu, X.-Y. Disassembling 2D van der Waals crystals into macroscopic monolayers and reassembling into artificial lattices. *Science* **2020**, *367*, 903−906.
(168) Yao, K.; Finney, N. R.; Zhang, J.; Moore, S. L.; Xian, L.; Tancogne-Dejean, N.; Liu, F.; Ardelean, J.; Xu, X.; Halbertal, D.; et al. Enhanced tunable second harmonic generation from twistable interfaces and vertical superlattices in boron nitride homostructures. *Sci. Adv.* **2021**, *7*, eabe8691.
(169) Zhang, W.; Hao, H.; Lee, Y.; Zhao, Y.; Tong, L.; Kim, K.; Liu, N. One Interlayer Twisted Multilayer MoS_2 Moiré Superlattices. *Adv. Funct. Mater.* **2022**, *32*, 2111529.
(170) Fan, X.; Jiang, Y.; Zhuang, X.; Liu, H.; Xu, T.; Zheng, W.; Fan, P.; Li, H.; Wu, X.; Zhu, X.; Zhang, Q.; Zhou, H.; Hu, W.; Wang, X.; Sun, L.; Duan, X.; Pan, A. Broken Symmetry Induced Strong Nonlinear Optical Effects in Spiral WS_2 Nanosheets. *ACS Nano* **2017**, *11*, 4892−4898.
(171) Feng, Q.; Zhu, M.; Zhao, Y.; Liu, H.; Li, M.; Zheng, J.; Xu, H.; Jiang, Y. Chemical vapor deposition growth of sub-centimeter single crystal WSe_2 monolayer by NaCl-assistant. *Nanotechnol* **2019**, *30*, 034001.
(172) Zhao, Y.; Zhang, C.; Kohler, D. D.; Scheeler, J. M.; Wright, J. C.; Voyles, P. M.; Jin, S. Supertwisted spirals of layered materials enabled by growth on non-Euclidean surfaces. *Science* **2020**, *370*, 442−445.
(173) Zhang, Z.; Chen, P.; Duan, X.; Zang, K.; Luo, J.; Duan, X. Robust epitaxial growth of two-dimensional heterostructures, multiheterostructures, and superlattices. *Science* **2017**, *357*, 788−792.
(174) Sahoo, P. K.; Memaran, S.; Xin, Y.; Balicas, L.; Gutiérrez, H. R. One-pot growth of two-dimensional lateral heterostructures via sequential edge-epitaxy. *Nature* **2018**, *553*, 63−67.
(175) Zhang, Z.; Huang, Z.; Li, J.; Wang, D.; Lin, Y.; Yang, X.; Liu, H.; Liu, S.; Wang, Y.; Li, B.; Duan, X.; Duan, X. Endoepitaxial growth of monolayer mosaic heterostructures. *Nat. Nanotechnol.* **2022**, *17*, 493−499.
(176) Li, J.; Yang, X.; Liu, Y.; Huang, B.; Wu, R.; Zhang, Z.; Zhao, B.; Ma, H.; Dang, W.; Wei, Z.; Wang, K.; Lin, Z.; Yan, X.; Sun, M.; Li, B.; Pan, X.; Luo, J.; Zhang, G.; Liu, Y.; Huang, Y.; Duan, X.; Duan, X. General synthesis of two-dimensional van der Waals heterostructure arrays. *Nature* **2020**, *579*, 368−374.
(177) Kim, K. S.; Lee, D.; Chang, C. S.; Seo, S.; Hu, Y.; Cha, S.; Kim, H.; Shin, J.; Lee, J. H.; Lee, S.; Kim, J. S.; Kim, K. H.; Suh, J. M.; Meng, Y.; Park, B. I.; Lee, J. H.; Park, H. S.; Kum, H. S.; Jo, M. H.; Yeom, G. Y.; Cho, K.; Park, J. H.; Bae, S. H.; Kim, J. Non-epitaxial single-crystal 2D material growth by geometric confinement. *Nature* **2023**, *614*, 88−94.
(178) Zhou, Z.; Hou, F.; Huang, X.; Wang, G.; Fu, Z.; Liu, W.; Yuan, G.; Xi, X.; Xu, J.; Lin, J.; Gao, L. Stack growth of wafer-scale van der Waals superconductor heterostructures. *Nature* **2023**, *621*, 499−505.
(179) Qiu, M.; Ren, W. X.; Jeong, T.; Won, M.; Park, G. Y.; Sang, D. K.; Liu, L. P.; Zhang, H.; Kim, J. S. Omnipotent phosphorene: a next-generation, two-dimensional nanoplatform for multidisciplinary biomedical applications. *Chem. Soc. Rev.* **2018**, *47*, 5588−5601.
(180) Tao, W.; Kong, N.; Ji, X.; Zhang, Y.; Sharma, A.; Ouyang, J.; Qi, B.; Wang, J.; Xie, N.; Kang, C.; Zhang, H.; Farokhzad, O. C.; Kim, J. S. Emerging two-dimensional monoelemental materials (Xenes) for biomedical applications. *Chem. Soc. Rev.* **2019**, *48*, 2891−2912.

https://doi.org/10.1021/prechem.3c00122
Precis. Chem. 2024, 2, 330−354

(181) Xu, Y.; Shi, X.; Zhang, Y.; Zhang, H.; Zhang, Q.; Huang, Z.; Xu, X.; Guo, J.; Zhang, H.; Sun, L.; Zeng, Z.; Pan, A.; Zhang, K. Epitaxial nucleation and lateral growth of high-crystalline black phosphorus films on silicon. *Nat. Commun.* **2020**, *11*, 1330.
(182) Akhtar, M.; Anderson, G.; Zhao, R.; Alruqi, A.; Mroczkowska, J. E.; Sumanasekera, G.; Jasinski, J. B. Recent advances in synthesis, properties, and applications of phosphorene. *npj 2D Mater. Appl.* **2017**, *1*, 5.
(183) Molle, A.; Goldberger, J.; Houssa, M.; Xu, Y.; Zhang, S. C.; Akinwande, D. Buckled two-dimensional Xene sheets. *Nat. Mater.* **2017**, *16*, 163−169.
(184) Zhang, L.; Huang, H.; Zhang, B.; Gu, M.; Zhao, D.; Zhao, X.; Li, L.; Zhou, J.; Wu, K.; Cheng, Y.; Zhang, J. Structure and properties of violet phosphorus and its phosphorene exfoliation. *Angew. Chem.* **2020**, *132*, 1090−1096.
(185) Ma, X.; Pan, H.; Yang, T.; Liao, Q.; Zhang, J.; Li, D. Optical Absorption and Second Harmonic Generation in Violet Phosphorene: Experimental and Theoretical Aspects. *Adv. Opt. Mater.* **2023**, *11*, 2202770.
(186) Cui, C.; Hu, W. J.; Yan, X.; Addiego, C.; Gao, W.; Wang, Y.; Wang, Z.; Li, L.; Cheng, Y.; Li, P.; Zhang, X.; Alshareef, H. N.; Wu, T.; Zhu, W.; Pan, X.; Li, L. J. Intercorrelated In-Plane and Out-of-Plane Ferroelectricity in Ultrathin Two-Dimensional Layered Semiconductor In_2Se_3. *Nano Lett.* **2018**, *18*, 1253−1258.
(187) Xie, S.; Dey, A.; Yan, W.; Kudrynskyi, Z. R.; Balakrishnan, N.; Makarovsky, O.; Kovalyuk, Z. D.; Castanon, E. G.; Kolosov, O.; Wang, K.; Patanè, A. Ferroelectric semiconductor junctions based on graphene/In_2Se_3/graphene van der Waals heterostructures. *2D Mater.* **2021**, *8*, 045020.
(188) Jacobs-Gedrim, R. B.; Shanmugam, M.; Jain, N.; Durcan, C. A.; Murphy, M. T.; Murray, T. M.; Matyi, R. J.; Moore, R. L.; Yu, B. Extraordinary photoresponse in two-dimensional In_2Se_3 nanosheets. *ACS Nano* **2014**, *8*, 514−521.
(189) Lin, S.; Zhang, G.; Lai, Q.; Fu, J.; Zhu, W.; Zeng, H. Recent Advances in Layered Two Dimensional Ferroelectrics from Material to Device. *Adv. Funct. Mater.* **2023**, *33*, 2304139.
(190) Zhang, F.; Wang, Z.; Dong, J.; Nie, A.; Xiang, J.; Zhu, W.; Liu, Z.; Tao, C. Atomic-Scale Observation of Reversible Thermally Driven Phase Transformation in 2D In_2Se_3. *ACS Nano* **2019**, *13*, 8004−8011.
(191) Claro, M. S.; Grzonka, J.; Nicoara, N.; Ferreira, P. J.; Sadewasser, S. Wafer-scale fabrication of fast two-dimensional β-In_2Se_3 photodetectors. *Adv. Opt. Mater.* **2021**, *9*, 2001034.
(192) Zhou, J.; Zeng, Q.; Lv, D.; Sun, L.; Niu, L.; Fu, W.; Liu, F.; Shen, Z.; Jin, C.; Liu, Z. Controlled Synthesis of High-Quality Monolayered alpha-In_2Se_3 via Physical Vapor Deposition. *Nano Lett.* **2015**, *15*, 6400−6405.
(193) Feng, W.; Zheng, W.; Gao, F.; Chen, X.; Liu, G.; Hasan, T.; Cao, W.; Hu, P. Sensitive Electronic-Skin Strain Sensor Array Based on the Patterned Two-Dimensional α-In_2Se_3. *Chem. Mater.* **2016**, *28*, 4278−4283.
(194) He, Q.; Tang, Z.; Dai, M.; Shan, H.; Yang, H.; Zhang, Y.; Luo, X. Epitaxial Growth of Large Area Two-Dimensional Ferroelectric alpha-In_2Se_3. *Nano Lett.* **2023**, *23*, 3098−3105.
(195) Sarkar, A. S.; Stratakis, E. Recent Advances in 2D Metal Monochalcogenides. *Adv. Sci.* **2020**, *7*, 2001655.
(196) Li, F.; Wang, H.; Huang, R.; Chen, W.; Zhang, H. Recent Advances in SnSe Nanostructures beyond Thermoelectricity. *Adv. Funct. Mater.* **2022**, *32*, 2200516.
(197) Wang, J.; Ronneberger, I.; Zhou, L.; Lu, L.; Deringer, V. L.; Zhang, B.; Tian, L.; Du, H.; Jia, C.; Qian, X.; et al. Unconventional two-dimensional germanium dichalcogenides. *Nanoscale* **2018**, *10*, 7363−7368.
(198) Tian, Z.; Guo, C.; Zhao, M.; Li, R.; Xue, J. Two-Dimensional SnS: A Phosphorene Analogue with Strong In-Plane Electronic Anisotropy. *ACS Nano* **2017**, *11*, 2219−2226.
(199) Xia, F.; Wang, H.; Hwang, J. C. M.; Neto, A. H. C.; Yang, L. Black phosphorus and its isoelectronic materials. *Nat. Rev. Phys.* **2019**, *1*, 306−317.
(200) Gao, Y.; Zhang, L.; Yao, G.; Wang, H. Unique mechanical responses of layered phosphorus-like group-IV monochalcogenides. *J. Appl. Phys.* **2019**, *125*, 082519.
(201) Wang, H.; Qian, X. Two-dimensional multiferroics in monolayer group IV monochalcogenides. *2D Mater.* **2017**, *4*, 015042.
(202) Zhao, L.-D.; Tan, G.; Hao, S.; He, J.; Pei, Y.; Chi, H.; Wang, H.; Gong, S.; Xu, H.; Dravid, V. P.; et al. Ultrahigh power factor and thermoelectric performance in hole-doped single-crystal SnSe. *Science* **2016**, *351*, 141−144.
(203) Zhao, L. D.; Lo, S. H.; Zhang, Y.; Sun, H.; Tan, G.; Uher, C.; Wolverton, C.; Dravid, V. P.; Kanatzidis, M. G. Ultralow thermal conductivity and high thermoelectric figure of merit in SnSe crystals. *Nature* **2014**, *508*, 373−377.
(204) Zhang, S.; Liu, S.; Huang, S.; Cai, B.; Xie, M.; Qu, L.; Zou, Y.; Hu, Z.; Yu, X.; Zeng, H. Structural and electronic properties of atomically thin germanium selenide polymorphs. *Sci. China Mater.* **2015**, *58*, 929−935.
(205) Hu, X.; Huang, P.; Liu, K.; Jin, B.; Zhang, X.; Zhang, X.; Zhou, X.; Zhai, T. Salt-Assisted Growth of Ultrathin GeSe Rectangular Flakes for Phototransistors with Ultrahigh Responsivity. *ACS Appl. Mater. Interfaces* **2019**, *11*, 23353−23360.
(206) Yoo, C.; Adepu, V.; Han, S. S.; Kim, J. H.; Shin, J.-C.; Cao, J.; Park, J.; Al Mahfuz, M. M.; Tetard, L.; Lee, G.-H.; Ko, D.-K.; Sahatiya, P.; Jung, Y. Low-Temperature Centimeter-Scale Growth of Layered 2D SnS for Piezoelectric Kirigami Devices. *ACS Nano* **2023**, *17*, 20680−20688.
(207) Blonsky, M. N.; Zhuang, H. L.; Singh, A. K.; Hennig, R. G. Ab initio prediction of piezoelectricity in two-dimensional materials. *ACS Nano* **2015**, *9*, 9885−9891.
(208) Zhao, C.; Li, Z.; Tang, T.; Sun, J.; Zhan, W.; Xu, B.; Sun, H.; Jiang, H.; Liu, K.; Qu, S.; Wang, Z.; Wang, Z. Novel III-V semiconductor epitaxy for optoelectronic devices through two-dimensional materials. *Prog. Quantum Electron.* **2021**, *76*, 100313.
(209) Zeng, F.; An, J.; Zhou, G.; Li, W.; Wang, H.; Duan, T.; Jiang, L.; Yu, H. A Comprehensive Review of Recent Progress on GaN High Electron Mobility Transistors: Devices, Fabrication and Reliability. *Electron.* **2018**, *7*, 377.
(210) Hong, N.; Geum, D.-M.; Kim, T. S.; Ahn, S.-y.; Han, J.-H.; Jung, D.; Ryu, G.; Kim, S.; Yu, K. J.; Choi, W. J. Flexible GaAs Photodetectors with Ultrathin Thermally Grown Silicon Dioxide as a Long Lived Barrier for Chronic Biomedical Implants. *Adv. Photonics Res.* **2021**, *2*, 2000051.
(211) Alaal, N.; Roqan, I. S. Tuning the Electronic Properties of Hexagonal Two-Dimensional GaN Monolayers via Doping for Enhanced Optoelectronic Applications. *ACS Appl. Nano Mater.* **2019**, *2*, 202−213.
(212) Chung, K.; Lee, C.-H.; Yi, G.-C. Transferable GaN layers grown on ZnO-coated graphene layers for optoelectronic devices. *Science* **2010**, *330*, 655−657.
(213) Alaskar, Y.; Arafin, S.; Wickramaratne, D.; Zurbuchen, M. A.; He, L.; McKay, J.; Lin, Q.; Goorsky, M. S.; Lake, R. K.; Wang, K. L. Towards van der Waals Epitaxial Growth of GaAs on Si using a Graphene Buffer Layer. *Adv. Funct. Mater.* **2014**, *24*, 6629−6638.
(214) Velicky, M.; Toth, P. S.; Rakowski, A. M.; Rooney, A. P.; Kozikov, A.; Woods, C. R.; Mishchenko, A.; Fumagalli, L.; Yin, J.; Zolyomi, V.; Georgiou, T.; Haigh, S. J.; Novoselov, K. S.; Dryfe, R. A. Exfoliation of natural van der Waals heterostructures to a single unit cell thickness. *Nat. Commun.* **2017**, *8*, 14410.
(215) Molina-Mendoza, A. J.; Giovanelli, E.; Paz, W. S.; Nino, M. A.; Island, J. O.; Evangeli, C.; Aballe, L.; Foerster, M.; van der Zant, H. S.; Rubio-Bollinger, G.; Agrait, N.; Palacios, J. J.; Perez, E. M.; Castellanos-Gomez, A. Franckeite as a naturally occurring van der Waals heterostructure. *Nat. Commun.* **2017**, *8*, 14409.
(216) Li, H.; Wu, X.; Liu, H.; Zheng, B.; Zhang, Q.; Zhu, X.; Wei, Z.; Zhuang, X.; Zhou, H.; Tang, W.; Duan, X.; Pan, A. Composition-Modulated Two-Dimensional Semiconductor Lateral Heterostructures via Layer-Selected Atomic Substitution. *ACS Nano* **2017**, *11*, 961−967.
(217) Yang, Y.; Liu, J.; Zhao, C.; Liang, Q.; Dong, W.; Shi, J.; Wang, P.; Kong, D.; Lv, L.; Jia, L.; Wang, D.; Huang, C.; Zheng, S.; Wang, M.; Liu,

F.; Yu, P.; Qiao, J.; Ji, W.; Zhou, J. A Universal Strategy for Synthesis of 2D Ternary Transition Metal Phosphorous Chalcogenides. *Adv. Mater.* **2023**, 2307237.
(218) Shu, Z.; Peng, Q.; Huang, P.; Xu, Z.; Suleiman, A. A.; Zhang, X.; Bai, X.; Zhou, X.; Zhai, T. Growth of Ultrathin Ternary Teallite ($PbSnS_2$) Flakes for Highly Anisotropic Optoelectronics. *Matter* **2020**, *2*, 977−987.
(219) Wang, J. P.; Fang, Y. Q.; He, W.; Liu, Q.; Fu, J. R.; Li, X. Y.; Liu, Y.; Gao, B.; Zhen, L.; Xu, C. Y.; et al. Non Centrosymmetric 2D Nb_3SeI_7 with High In Plane Anisotropy and Optical Nonlinearity. *Adv. Opt. Mater.* **2023**, *11*, 2300031.
(220) Briggs, N.; Subramanian, S.; Lin, Z.; Li, X.; Zhang, X.; Zhang, K.; Xiao, K.; Geohegan, D.; Wallace, R.; Chen, L.-Q.; Terrones, M.; Ebrahimi, A.; Das, S.; Redwing, J.; Hinkle, C.; Momeni, K.; van Duin, A.; Crespi, V.; Kar, S.; Robinson, J. A. A roadmap for electronic grade 2D materials. *2D Mater.* **2019**, *6*, 022001.
(221) Jang, A. R.; Hong, S.; Hyun, C.; Yoon, S. I.; Kim, G.; Jeong, H. Y.; Shin, T. J.; Park, S. O.; Wong, K.; Kwak, S. K.; Park, N.; Yu, K.; Choi, E.; Mishchenko, A.; Withers, F.; Novoselov, K. S.; Lim, H.; Shin, H. S. Wafer-Scale and Wrinkle-Free Epitaxial Growth of Single-Orientated Multilayer Hexagonal Boron Nitride on Sapphire. *Nano Lett.* **2016**, *16*, 3360−3366.
(222) Zeng, F.; Wang, R.; Wei, W.; Feng, Z.; Guo, Q.; Ren, Y.; Cui, G.; Zou, D.; Zhang, Z.; Liu, S.; Liu, K.; Fu, Y.; Kou, J.; Wang, L.; Zhou, X.; Tang, Z.; Ding, F.; Yu, D.; Liu, K.; Xu, X. Stamped production of single-crystal hexagonal boron nitride monolayers on various insulating substrates. *Nat. Commun.* **2023**, *14*, 6421.
(223) Mondal, A.; Biswas, C.; Park, S.; Cha, W.; Kang, S. H.; Yoon, M.; Choi, S. H.; Kim, K. K.; Lee, Y. H. Low Ohmic contact resistance and high on/off ratio in transition metal dichalcogenides field-effect transistors via residue-free transfer. *Nat. Nanotechnol.* **2024**, 1497.
(224) Qin, B.; Saeed, M. Z.; Li, Q.; Zhu, M.; Feng, Y.; Zhou, Z.; Fang, J.; Hossain, M.; Zhang, Z.; Zhou, Y.; Huangfu, Y.; Song, R.; Tang, J.; Li, B.; Liu, J.; Wang, D.; He, K.; Zhang, H.; Wu, R.; Zhao, B.; Li, J.; Liao, L.; Wei, Z.; Li, B.; Duan, X.; Duan, X. General low-temperature growth of two-dimensional nanosheets from layered and nonlayered materials. *Nat. Commun.* **2023**, *14*, 304.
(225) Hoang, A. T.; Hu, L.; Kim, B. J.; Van, T. T. N.; Park, K. D.; Jeong, Y.; Lee, K.; Ji, S.; Hong, J.; Katiyar, A. K.; Shong, B.; Kim, K.; Im, S.; Chung, W. J.; Ahn, J. H. Low-temperature growth of MoS_2 on polymer and thin glass substrates for flexible electronics. *Nat. Nanotechnol.* **2023**, *18*, 1439−1447.
(226) Xu, X.; Liu, K. Progress and perspective on the growth of two-dimensional single crystals. *Sci. Bull.* **2022**, *67*, 1410−1412.
(227) Ci, L.; Song, L.; Jin, C.; Jariwala, D.; Wu, D.; Li, Y.; Srivastava, A.; Wang, Z. F.; Storr, K.; Balicas, L.; Liu, F.; Ajayan, P. M. Atomic layers of hybridized boron nitride and graphene domains. *Nat. Mater.* **2010**, *9*, 430−435.
(228) Wang, X.; Yasuda, K.; Zhang, Y.; Liu, S.; Watanabe, K.; Taniguchi, T.; Hone, J.; Fu, L.; Jarillo-Herrero, P. Interfacial ferroelectricity in rhombohedral-stacked bilayer transition metal dichalcogenides. *Nat. Nanotechnol.* **2022**, *17*, 367−371.
(229) Wu, Y.; Li, D.; Wu, C.-L.; Hwang, H. Y.; Cui, Y. Electrostatic gating and intercalation in 2D materials. *Nat. Rev. Mater.* **2023**, *8*, 41−53.
(230) Zhu, K.; Pazos, S.; Aguirre, F.; Shen, Y.; Yuan, Y.; Zheng, W.; Alharbi, O.; Villena, M. A.; Fang, B.; Li, X.; Milozzi, A.; Farronato, M.; Munoz-Rojo, M.; Wang, T.; Li, R.; Fariborzi, H.; Roldan, J. B.; Benstetter, G.; Zhang, X.; Alshareef, H. N.; Grasser, T.; Wu, H.; Ielmini, D.; Lanza, M. Hybrid 2D-CMOS microchips for memristive applications. *Nature* **2023**, *618*, 57−62.
(231) Qiu, D.; Gong, C.; Wang, S.; Zhang, M.; Yang, C.; Wang, X.; Xiong, J. Recent Advances in 2D Superconductors. *Adv. Mater.* **2021**, *33*, 2006124.
(232) Meng, P.; Wu, Y.; Bian, R.; Pan, E.; Dong, B.; Zhao, X.; Chen, J.; Wu, L.; Sun, Y.; Fu, Q.; Liu, Q.; Shi, D.; Zhang, Q.; Zhang, Y. W.; Liu, Z.; Liu, F. Sliding induced multiple polarization states in two-dimensional ferroelectrics. *Nat. Commun.* **2022**, *13*, 7696.
(233) Mueller, T.; Malic, E. Exciton physics and device application of two-dimensional transition metal dichalcogenide semiconductors. *npj 2D Mater. Appl.* **2018**, *2*, 29.
(234) Bian, R.; Li, C.; Liu, Q.; Cao, G.; Fu, Q.; Meng, P.; Zhou, J.; Liu, F.; Liu, Z. Recent progress in the synthesis of novel two-dimensional van der Waals materials. *Natl. Sci. Rev.* **2022**, *9*, nwab164.

https://doi.org/10.1021/prechem.3c00122
Precis. Chem. 2024, 2, 330−354